DOI 10.1002/2015GC006034

Composition, geometry and emplacement dynamics of a large volcanic island landslide offshore Martinique: from volcano flank-collapse to seafloor sediment failure?

Morgane Brunet*[1], Anne Le Friant[1], Georges Boudon[1], Sara Lafuerza[1], Peter Talling[2], Matthew Hornbach[3], Osamu Ishizuka[4], Elodie Lebas[5], Hervé Guyard[1] and IODP Expedition 340 science party

1 : Institut de Physique du Globe de Paris, Sorbonne Paris Cité, Université Paris Diderot, CNRS UMR 7154, 1, rue Jussieu, Paris, France.

2: National Oceanography Center, University of Southampton, Southampton, UK

3: Department of Earth Sciences, Southern Methodist University, Dallas, Texas, USA

4: Geological Survey of Japan, AIST, Tsukuba, Japan

5: Geomar Helmholtz Centre for Ocean Research, Kiel, Germany

First author contact address:

Mrs. Morgane Brunet

Institut de Physique du Globe de Paris

Laboratoire des Systèmes Volcaniques

1 rue Jussieu

75238 Paris

France

mbrunet@ipgp.fr

+33 (0) 1 83 95 76 38

Key points:

- First drilling into submarine landslide deposits offshore volcanic island
- Large (300 km^3) submarine landslide deposit offshore Martinique comprises mainly deformed seafloor sediment, in a single frontally emergent morphology

Received: Jul 31, 2015; Revised: Nov 03, 2015; Accepted: Nov 16, 2015

Abstract

Landslides are common features in the vicinity of volcanic islands. In this contribution, we investigate landslides emplacement and dynamics around the volcanic island of Martinique based on the first scientific drilling of such deposits. The evolution of the active Montagne Pelée volcano on this island has been marked by three major flank-collapses that removed much of the western flank of the volcano. Subaerial collapse volumes vary from 2 to 25 km^3 and debris avalanches flowed into the Grenada Basin. High-resolution seismic data (AGUADOMAR – 1999, CARAVAL – 2002 and GWADASEIS – 2009) is combined with new drill cores that penetrate up to 430 m through the three submarine landslide deposits previously associated to the aerial flank-collapses (Site U1399, Site U1400, Site U1401, IODP Expedition 340, Joides Resolution, March-April 2012). This combined geophysical and core data provide an improved understanding of landslide processes offshore a volcanic island. The integrated analysis shows a large submarine landslide deposit, without debris avalanche deposits coming from the volcano, comprising up to 300 km^3 of remobilized seafloor sediment that extends for 70 km away from the coast and covers an area of 2100 km^2. Our new data suggest that the aerial debris avalanche deposit enter the sea but stop at the base of submarine flank. We propose a new model dealing with seafloor sediment failures and landslide propagation mechanisms, triggered by volcanic flank-collapse events affecting Montagne Pelée volcano. Newly recognized landslide deposits occur deeper in the stratigraphy, suggesting the recurrence of large-scale mass-wasting processes offshore the island and thus, the necessity to better assess the associated tsunami hazards in the region.

1. Introduction

Flank-instabilities are a recurrent process in the long-term evolution of many volcanoes [*Siebert*, 1984; *McGuire*, 1996]. Exceptionally large volcanic landslides have been recognized offshore oceanic intraplate islands such as Hawaii [*Moore et al*., 1989, *Moore et al.*, 1994], the Canary Islands [*Carracedo*, 1999; *Masson et al.*, 2002], La Réunion Island [*Labazuy*, 1996; *Oehler et al.*, 2004, 2008] and in subduction zones such as the Lesser Antilles [*Deplus et al*., 2001; *Le Friant et al*., 2003a,b; *Boudon et al*., 2007]. The scale of some of these events exceeds the largest-known, subaerial volcanic landslide [e.g. Mount Shasta deposit > 45 km^3, *Crandell et al*., 1989], as landslide deposit volumes offshore Hawaii exceed 5000 km^3 [*Moore et al*., 1994, *Masson et al*., 2002]. Volcano flank-collapses generate typical horseshoe-shaped structures on land, and the resulting debris avalanches can flow downslope several tens of kilometers. The sudden entrance of voluminous debris avalanches into the sea can trigger complex submarine mass-movements [*Bull et al*., 2009; *Gee et al*., 2005; *Le Friant et al*., 2015; *Watt et al*., 2014] as well as catastrophic tsunamis [*Harbitz et al*., 2012]. The magnitude of such tsunamis is a source of debate [*Ward and Day*, 2001, *Ward*, 2001], as it is directly related to landslide emplacement processes [*Watt et al*. 2012]. There are no detailed direct monitoring observations of a large volcanic island landslide in action. Thus, it remains unclear how submarine landslide emplacement occurs because of significant uncertainties concerning its dynamics. However, previous studies have provided some insightful concepts on the dynamic emplacement of submarine landslides, especially from the resulting deposits's geometry. For instance, *Frey-Martinez et al*., [2005, 2006] were the first to define two categories of submarine landslides morphologies, so-called "frontally confined" and "frontally emergent". Both are characterized by specific structural features (i.e. emergent frontal ramp for the later) that are relevant of emplacement kinetic. Others kinematics or morphological indicators exist and are widely described in others studies [*Bull et al.*, 2011; *Watt et al*., 2012a, 2014]. Moreover, a series of conceptual models have been proposed by previous work for down slope propagation of submarine deformation offshore volcanic islands [*Watt et al*., 2012; *Le Friant et al*., 2015], such as erosion and loading of seafloor-sediment by volcanic debris avalanche, loading of seafloor-sediment by an overrunning volcanic debris flow, self-loading by down-slope propagating seafloor-sediment failures, or long-distance decollement propagation from the site debris avalanche loading. These models

demonstrate the large-scale of submarine processes that may occur in relation to aerial instabilities processes, and especially in volcanic island contexts.

Montagne Pelée volcano in Martinique (Lesser Antilles Arc, Figure 1) has experienced three major flank-collapse events during the last ~130 Ma years, which removed much of the western flank of the volcano [*Le Friant et al*., 2003a; *Boudon et al*., 2005, 2007]. Previous geophysical and geological investigations allowed *Le Friant et al*. [2003a] to identify and to map three submarine deposits, which they correlated with the three major subaerial flank-collapse events (Figure 2). Le Friant et al. [2015] proposed that the largest deposit offshore Martinique mainly comprises seafloor-sediments rather than debris avalanche deposits from the volcanic edifice, based on the first ever scientific drilling of volcanic landslides during IODP Expedition 340 in 2012. However, the limited resolution and coverage of the seismic data used previously, hampered the analysis of these submarine landslide deposits and their emplacement processes. Higher resolution seismic reflection data had been collected in 2002 (CARAVAL cruise, 24 channels) and 2009 (GWADASEIS cruise, 72 channels), but they have never been analyzed together with AGUADOMAR cruise data to provide a more complete understanding of mass-movement processes. This set of seismic data consists of ~1200 kilometers of multichannel lines. When combined with IODP cores collected during the IODP Expedition 340 (Figure 2), the data provide key insights into the understanding of volcanic landslide processes in an oceanic context.

1.1. Aims

During IODP Expedition 340, large submarine landslide deposits associated with the island volcanic activity were drilled for the first time [e.g. *Le Friant et al*., 2015]. It offers a unique opportunity to improve our understanding of submarine landslides, by addressing the following questions: What is the spatial extent of landslide processes off Montagne Pelée? Can we quantify the volume and distribution of volcanic material that enter the sea? What are the types and mechanisms of submarine landslides? What is the geometry of resulting deposits? What is the link between volcano flank-collapses and submarine mass-movements? Therefore, the aim of this paper is to investigate landslide composition and emplacement processes off Montagne Pelée, using the complete marine geophysical data set collected during the three oceanographic cruises mentioned above, and combined with the unique deep

cores gathered during IODP Expedition 340 [*e.g. Wall-Palmer et al.,* 2014; *Le Friant et al*., 2013, 2015]. We first redefine the extents of previously identified deposits [*Le Friant et al*., 2003a] and highlight new deeper landslide deposits. Then, we discuss the characteristic features (architecture, composition, deformation and distribution), types and origins of submarine landslide deposits. Finally, we propose a new model for landslide processes offshore Martinique, linking subaerial instability processes (i.e. volcano flank-collapse events) and submarine instability processes (i.e. seafloor sediment failure), and discuss emplacement and timing of landslides in the history of Montagne Pelée volcano.

1.2. Terminology

In this contribution, *landslide* is used as a general term for any type of slope failure and resulting mass-movement. The term *debris avalanche* is used for a failure containing cohesionless rock fragments from the volcanic edifice [*Masson et al*., 2002, 2006; *Watt et al*., 2014], which may include the *terrestrial flank* or *submarine flank* of the volcano. Debris avalanches are distinguished from *slumps* in that involve discrete fault-bounded movements with basal slip surfaces [e.g. *Delcamp et al*., 2008]. *Debris flows* comprise disaggregated and remolded material with high-sediment concentrations [*Iverson et al*., 1997], whilst *turbidity currents* are more diluted sediment flows [*Talling et al*., 2012]. In this study, resulting deposits are thick (> 2m) massive sand layers, dominated by volcanic material. *Hemipelagic sediment* deposited mainly background fallout of sediment from the ocean. It comprises mud-dominated intervals with variable amounts of disseminated sand [*Trofimovs et al*., 2013]. Both turbidity currents and fallout (tephra) from volcanic eruptions can generate thin (typically a few cm) normally-graded silt or sand layers, which can be problematic to distinguish [*Cassidy et al*., 2014]. It is also possible that thinner eruption fallout or turbidite layers become pervasively bioturbated, such that they are no longer recognizable. Better-sorted layers are considered to be tephra fallout for the purposes of this study. Distinctive intervals of structureless and uniform (homogenized) intervals of sandy mud (usually 1 to 8 m thick), with a distinctly higher sand content than pure hemipelagite are called *homogenized sandy-mud layers*. Finally, failures of well-bedded seafloor-sediment, located at the slope break marking the base of the volcanic edifice, are referred to *seafloor-sediment failures*.

2. Geological context and previous data

Martinique is part of the Lesser Antilles Arc and results from the subduction of the Atlantic oceanic crust beneath the Caribbean Plate, at a relatively slow rate of 2 cm/yr [*Wadge*, 1984]. The arc is curved toward the Atlantic, and extends for over 800 km from South America to the Greater Antilles. Arc volcanism started 40 million years ago [*Martin-Kaye*, 1969; *Bouysse et al*., 1990] and has progressively migrated to the southwest, leading to the formation of two distinct arcs to the north of Dominica (Figure 1). The outer arc corresponds to the older part, where thick coral reef platforms cover volcanic basement, while the inner arc includes all volcanoes active in the last 20 Ma [*Bouysse et al*., 1990]. South of Dominica, the arc is composed of only one arc, where ancient and current volcanisms are superimposed. The arc is bordered to the west by the 2900 m deep back-arc Grenada Basin. Martinique is located where the two arcs bifurcate. Its active volcanic centers have progressively migrated from southeast to northwest of the island, since the early Miocene.

Montagne Pelée is located in the northern part of Martinique, and it is the island's only active volcano during the last 300 Ma. Sadly, it is a well-known volcano for the tragic 1902 – 1905 eruptions that destroyed the towns of St. Pierre and Morne Rouge, and killed 30 000 inhabitants [*Lacroix*, 1904].

2.1. Subaerial volcano flank-collapse features

During its evolution, the volcano has experienced at least three major flank-collapse events, with subaerial collapse volumes estimated from 2 to 25 km^3 [*Le Friant et al.*, 2003a, *Boudon et al*., 2005, 2007]. On-land investigations, combined with aerial photos and hydrographic system analyses, indicate the presence of three horseshoe-shaped structures opening to the southwest (Figure 2).

The first terrestrial flank-collapse event was dated as older than 127 ± 2 ka using K-Ar dating techniques, with samples from pre- and post-collapse lavas emplaced across the collapse structure, [*Germa et al*., 2011]. This is the largest identified collapse event (8 x 6 km horseshoe-shaped structure), corresponding to a missing volume of 25 km^3 [*Le Friant et al*., 2003a].

The second terrestrial flank-collapse event was dated at 32 ka ± 2 ka [*Boudon et al*., 2013] and formed a horseshoe-shaped structure that is 6.5 by 4 km in size. This age is based on ^{14}C dates on charcoal included inside pyroclastic deposits filling the structure, and $\delta^{18}O$ stratigraphy obtained on a piston core located at the northwest of Montagne Pelée. A missing volume of 13 km^3 was estimated. However, this age is still uncertain, and the second flank-collapse event may have occurred earlier, between 45-127 ka [*Le Friant et al*, 2015].

Finally, U-Th disequilibrium dating of lava domes emplaced before and after the flank-collapse was used to date the most recent subaerial flank-collapse event [*Le Friant et al*, 2003a]. This third event was previously dated at ~ 9 ka, but new constraints provided by IODP drill site U1401 [*Le Friant et al.*, 2015] suggested older ages for the associated deposit (30-45 ka). It is the smallest of the three subaerial collapses, with a horseshoe-shaped structure of 1.5 by 4 km, and missing volume of 2 km^3.

2.2. Submarine landslide deposits (D1, D2 and D3)

Swath bathymetry and seismic reflection data acquired during the AGUADOMAR cruise (1999) offshore west of Montagne Pelée, revealed the presence of three large submarine deposits (D1, D2 and D3) aligned with the three on-land flank-collapse structures (Figure 2). *Le Friant et al*. [2003a] previously inferred a correlation between the three subaerial collapse events, and the three submarine landslide deposits. The latter were interpreted as a mix of debris avalanche deposits and incorporated marine sediments.

Submarine deposit D1 extends for 70 km from the coastline, and covers an area of 1100 km^2. It was previously linked to the first subaerial collapse event [*Le Friant et al*., 2003a]. D1 displays a smaller front in its southern part (Figure 2). Submarine deposit D2 extends for 50 km from the coastline, and covers an area of 700 km^2. D2 has a distinctive morphological front that is generally 10-20 m high and locally up to 35 m high. Deposit D2 was linked to the second subaerial collapse [*Le Friant et al*., 2003a]. Submarine deposit D3 differs from D1 and D2 is key regards. First, it is much smaller in size and volume, and is located at the base of the submarine flank. Second, it has a hummocky morphology and a lobate shape, with a morphological front (Figure 2). Third, megablocks, 100–500 m in diameter and 10–40 m high, are concentrated in the central part of the deposit (Figure 2). D3 was linked to the most recent subaerial collapse event [*Le Friant et al*., 2003a]. The blocky

nature of D3 may suggest that it comprises indurated blocks of volcanic material from the volcanic edifice.

More recently, *Le Friant et al. [2015]* suggest that D1 and D2 deposits could be related to seafloor-sediment failure rather than volcanic debris avalanche deposits. Linkages between these various subaerial collapses and submarine landslide deposits are subsequently re-analyzed by this contribution, and new estimates of the submarine landslide volumes are provided.

3. Materials and methods

3.1. Marine geophysical dataset

During the AGUADOMAR cruise (R/V L'*Atalante*, December 1998 - January 1999), Simrad EM12D swath bathymetry and backscatter data, 3.5 kHz echo sounder, gravity, magnetic and 6-channel seismic reflection profiles were collected from Montserrat to St. Vincent [*Deplus et al*. 2001]. The CARAVAL cruise (R/V L'*Atalante*) in 2002 collected seismic profiles using a 24-channel streamer [*Deplus et al*., 2002], together with piston cores and dredge samples (Figure 3). The GWADASEIS campaign (R/V *Le Suroît*) in 2009 gathered high-resolution seismic profiles using a 72-channel streamer, with additional piston cores. Navigation was achieved using Starfix differential GPS during the AGUADOMAR cruise, and using GPS with no degradation during the CARAVAL and GWADASEIS cruises. During the latter two cruises, this allowed a ship position accuracy of a few meters. Swath bathymetry and backscatter data were processed using the CARAIBES software developed by IFREMER. Digital elevation models were constructed with resolutions of 50, 100 and 200 m depending on the depth of the seafloor and mosaics of acoustic imagery. For the three cruises, the multichannel seismic reflection data were filtered, stacked and migrated after NMO correction, using the ‘‘Seismic Unix’’ software [*Cohen and Stockwell*, 1996].

Interpretation of the seismic reflection data from the AGUADOMAR, CARAVAL and GWADASEIS cruises was performed using Kingdom Suite© software. Twenty-one seismic profiles, with a total length of 1200 km, were acquired offshore Martinique as part of this

study (Figure 3). Thickness of sediments packages was calculated based on in-situ measurements of P-waves velocity obtained during IODP Expedition 340 (*see section 4.2)*. Volumes of deposits are estimated using subsurface seismic velocity estimates and Kingdom Suite© software, and taking into account lateral thickness variations of the deposits.

3.2. Sediment cores

IODP Expedition 340 (R/V *Joides Resolution*, March-April 2012) was held offshore Montserrat and Martinique islands [*Le Friant et al*., 2013, 2015]. At Site U1399, two holes were cored (U1399-A and U1399-B) while 3 holes were cored at Site U1400 (U1400-A, U1400-B and U1400-C). In this study, we focus on cores U1399-A and U1400-C because they are the most complete for each site (Table 1). Comparisons and correlations with the others holes were performed and are described in *section 4.3.2*.

The sediment cores were cut onboard into 1.5 m sections, and continuous physical properties such as P-wave velocities, density, NGR (natural gamma ray radiation) were then measured using a Wholeround Multisensor core logger (WRMSCL), before the cores were split. Digital images of the archive halves were captured using the Section Half Imaging Logger (SHIL), and high-resolution photographs were taken using a line scan camera at intervals of 20 pixels/mm. Measurements of magnetic susceptibility and color reflectance were performed with the Section Half Multisensor Logger (SHMSL) on the archive halves. Finally, sedimentological, magmatic and structural features were described.

CAT-Scan (Computerized Axial Tomography) analyses were carried out at the College of Veterinary Medicine of the Texas A&M University (College Station, USA), using a Siemens definition AS 40 slice CT Scanner that produces a 0.6 mm slice thickness. Data were processed using the Osirix software and the resulting longitudinal images are displayed in greyscale, with the darker grey representing lower X-ray attenuation and lower bulk density values [e.g. *Boespflug et al*., 1995; *Duliu*, 1999]. This nondestructive and high-resolution method allows especially to visualize and characterize deformation microstructures associated with the dynamic of sedimentary mass-movements [e.g. *Duliu*, 1999; *Guyard et al.*, 2014; *St-Onge et al*., 2008].

3.3. Downhole logging of physical properties

Downhole logs that measured in situ physical properties were acquired at Hole U1399-C. They were not acquired at Site U1400 because of unfavorable Holes conditions [see *Le Friant et al*., 2013]. Magnetic susceptibility, resistivity, bulk density, natural gamma radiation (NGR) were measured using the triple combination tool string, incorporating the Magnetic Susceptibility Sonde (MSS). NGR measurements help to identify clay and mud rich layers. Clay minerals that fix K, Th and U are the principal source of natural gamma radiation. Sonic velocities were measured using the Formation MicroScanner (FMS) sonic tool string. Finally, the Versatile Seismic Imager (VSI) was deployed to acquire a zero-offset Vertical Seismic Profile (VSP) for calibrating the integration of borehole and seismic data.

4. Results

We first outline the results of the combined geophysical data from the different cruises. This is then followed by results from our analyses of the newly acquired IODP cores.

4.1. Seismic data analysis

4.1.1. Seismic facies

Three seismic facies are observed west of Martinique that we term the chaotic, disturbed and well-bedded seismic facies (Figures 4 and S1). The chaotic facies is characterized by highly disrupted to very low amplitude reflectors (Figure 4b and Figure 4d). The disturbed facies shows discontinuous and deformed reflectors with relatively high amplitude (Figure 4c). Finally, a well-bedded facies is observed, displaying high-amplitude, continuous and subparallel reflectors (Figure 4a). This well-bedded facies represents undisturbed marine stratigraphy, and includes the undisturbed drape above the landslide deposits.

4.1.2. Deposits geometries and nomenclature

New data and interpretations provided in this contribution imply to change the terminology of the submarine deposits (previously named D1, D2 and D3 deposits) for the convenience of the reader. Seismic data collected during the CARAVAL cruise (Lines 16 and

17, Figure 3) reveal a continuum between deposits D1 and D2, with a basal surface that is continuous between both deposits. This single common surface is associated with a high amplitude reflector that extends downslope from the coastline for more than 70 km (Figures 4 and S1). Based on this apparent continuity of basal reflector, and by others characteristics (nature, deformation) that will be described in more details later in the text from the cores analysis, we proposed that D1 and D2 belong to the same deposit that we now refer to a single unit so called "SLD" for "*submarine landslide deposit"* (Figure 4 and S1). The D3 characteristics are broadly similar to those described by *Le Friant et al* [2003a] and in section 2.2. For clarification, we propose to call it DAD3 to refer to *debris avalanche deposit* 3.

4.1.3. The submarine landslide deposit (SLD)

The SLD extends for 72 km away from Martinique, covers an area of 2100 km^2, and has an estimated volume of ~ 300 km^3. The upper surface of SLD includes a major morphological front in its central part, and a smaller morphological front in its southeast part (Figures 2, 5 and 6). Using mean P-wave velocity values (Figure 7) measured in borehole U1399-A (1650 m/s) and U1400-C (1700 m/s), the thickness of the SLD was obtained, which varies from ~ 500 m within central part, to ~80 m within distal part. The SLD displays different seismic facies and morphological features from its proximal to its distal parts, which are now described (Figures 5 and 6).

4.1.3.1. Proximal unit of the SLD

The proximal part of the SLD lies on the steep submerged flanks of the volcanic edifice, ending at the slope break (Figures 3, 5 and 6). It is first visible at a distance of 10 - 14 km from the coastline. It extends for a further ~ 11-22 km, and is ~ 200-300 meters thick (Figures 5 and 6). On the CARAVAL-16 profile, a unit with relative continuous and parallel internal reflectors is seen, within chaotic seismic facies (Figure 5B). This proximal part of the SLD is covered by a thick sediment package, but diffraction hyperbola may suggest out-of-plane presence of volcanic blocks. No specific structure is identified within the chaotic seismic facies on the CARAVAL-17 profile, except at the upper limit of the slide that corresponds to the base of the DAD3 deposit. Relatively well-bedded reflectors are also recognized below the SLD (Figure 6).

4.1.3.2. Central unit of the SLD

The central part of the SLD extends from the slope break to a prominent morphological front (Figures 2 and 3). It is ~22 km long and 350 – 500 m thick, making the central unit the thickest part of the SLD (Figure 5). It is mainly characterized by a chaotic seismic facies (Figures 5 and 6). Seismic sections show a high amplitude, nearly continuous reflector at the base of the deposit, which separates chaotic facies from the well-bedded seismic facies below (Figure 5B). The basal reflector is initially near-parallel to the seabed. Further downslope, it becomes discontinuous, and ramps up to a higher stratigraphic level where it continues as a second flat basal surface. This ramp structure is 150 m high on the CARAVAL-16 profile, but it is absent on the CARAVAL-17 profile. It is located updip (CARAVAL-16) from the morphological front (Figures 5 and 6). This morphological front is identified both on CARAVAL-16 and CARAVAL-17 seismic profiles, as well as on swath bathymetry data (Figures 2, 5 and 6). Localized at 44-55 km from the coastline, it is 40 - 80 m high and 7 - 13 km long. The central part of the SLD contains tilted internal reflectors, which are inclined upwards on CARAVAL-16 and downward on CARAVAL-17 (Figures 5 and 6). It is also covered by a thick package of sediments characterized by high amplitude, flat-lying reflectors. The thickness of this overlying sediment drape ranges from ~10 m to ~70 m (Figures 5 and 6).

4.1.3.3. Distal unit of the SLD

The distal part of the SLD extends from the morphological front to the final distal limit of the deposit (Figure 3). This is the thinnest (125-150m) part of the SLD (Figures 5 and 6) and extends over ~25-28 km. A high-amplitude and continuous reflector is seen at the base of the SLD in this area, at ~220 mbsf. The strong basal reflector is near horizontal (Figures 5 and 6). The thickness of overlying sediment varies. Close to the morphological front, overlying sediment may reach a thickness of 60 to 70 m on both CARAVAL-16 and CARAVAL-17. Closer to the distal toe of the SLD, this overlying sediment drape is typically 30 - 40 m thick (Figures 5 and 6).

The chaotic-to-transparent seismic facies in the central part of the SLD evolves into a disturbed seismic facies in its distal part. The distal edge of the SLD has a more chaotic facies

(Figures 4, S1, 5B and 6B). Successive thrusts and folded reflectors are also recognized. Observed thrusts are arranged in an echelon manner, inclined upward on the CARAVAL-16 line and downward on the CARAVAL-17 line. Folded reflectors are observed at the most distal part of the unit, and between thrusts (Figure 5). These coupled thrust and fold structure affect the whole distal unit. Finally, the toe of the SLD is characterized by a sharp frontal truncation between the chaotic and the well-bedded seismic facies, with distributed deformation from highly disturbed reflectors to down-slope well-bedded strata (Figures 5 and 6).

4.1.4. The deeper submarine landslide deposits (SLDx)

Additional disturbed or chaotic facies are seen below the base of the SLD, between ~ 3.9 – 4.7 seconds twt. They are separated by well-bedded and high-amplitude reflectors from the SLD (Figures 4, S1, 5A and 6A). We term these landslides the SLDx deposits. The extent of SLDx landslides deposits is picked out well by the CARAVAL-16 and CARAVAL-17 seismic lines, but they are less clear on other seismic lines (Figure 3). Nevertheless, the SLDx landslide deposits extend just as far offshore as the SLD (Figures 5 and 6), but were not penetrated by the drilling during IODP Expedition 340.

4.2. Seismic velocities

Seismic velocities are used to convert two-way travel times into sediment thicknesses. They have been measured during the 340 IODP Expedition (Le Friant et al., 2013; 2015). At site U1399, P-waves velocities in volcanoclastic material range from 1650 to 1800 m/s, with lower velocities of 1500 to 1550 m/s in hemipelagite-dominated intervals. At site U1400, P-waves velocities within volcanoclastic sediment are also higher (1700 to 1840 m/s) than within hemipelagic sediments (1650 to 1750 m/s). A velocity model was established for each Hole using these P-wave velocity measurements (Figure 7), so that depth values are derived from the models formulas. Outliers with unusually high P-wave velocity in Hole U1399-A correspond to thick turbidity current deposits, which do not occur in Hole U1400-C (Figure 9).

4.3. Sedimentary lithofacies and physical properties

4.3.1. Physical properties data

Continuous measurements of bulk density exhibit higher values related to thick volcanoclastic deposits up to 2 cm^3. Magnetic susceptibility ranges between 1850 and 7015 10^{-5} SI, the latter being the highest value measured in volcanoclastic deposits. NGR measurements highlighting clayey and muddy layers, display values between 14.6 and 53.7 counts per second (cps) (Figure 8). Therefore, physical properties combined with visual core logging allow distinctions between hemipelagic sediments and volcanoclastic material including turbidity current deposits and tephra layers (Figures 8 and 9).

4.3.2. Site U1399 and U1400

The sequence of sediment types seen at Sites U1399 and U1400 is summarized in Figure 9. Each IODP drill site comprises a series of individual Holes (e.g. U1399-A and U1399-B) that are typically located only tens to several hundred of meters apart [*Le Friant et al*., 2013]. Some general correlations are possible between cores at each of the two sites. However, a striking feature is the variability of sediment sequence between adjacent cores over such short distances (Figure 9). Site U1399 has a much greater abundance of thick volcanoclastic turbidite sand layers, although this may be accentuated somewhat by suck-in of sand during piston coring [*Jutzeler et al*., 2014]. This is somewhat surprising, given that Site U1399 is located much further from Martinique than Site U1400 (Figure 2). Thicker turbidity current deposits might be expected in Site U1400, as it is the more proximal and shallower-water location. It is possible that the turbidity currents reached Site U1399 mainly from Dominica, via a north-south oriented submarine channel system. The homogenized muddy-sand lithofacies is well developed at Site U1399, but absent at Site U1400. These homogenized sandy-mud deposits may either represent debris flow deposits or post-depositional shearing along localized horizons. In either case, such a process only affected the more distal IODP Site U1399 (Figure 9).

4.4. Deformation

Several millimeters to centimeters scale deformation features (i.e. brittle, ductile and polyphase) are observed within both cores U1399-A and U1400-C, and are illustrated by

photographs and CT-scanning (Figure 10). According to the degree and complexity of deformation (e.g. tilt and the mix of different features), eight categories of deformations are defined (Figure 11). These categories are: 1/weakly inclined banding (< 45°), 2/ highly inclined banding (≥ 45°), 3/ weakly inclined and contorted bedding, 4/ highly inclined and contorted bedding, 5/ weakly inclined and contorted bedding in multi directions, 6/ highly inclined and contorted bedding in multi directions, 7/ alternation of highly/weakly inclined, and 8/ contorted bedding in multi directions and mixed layers.

Quantifications of deformations observed within cores U1399-A and U1400-C are summarized in Table 2. Unsuccessful coring, due to drilling issues, led to 21% of void within Hole U1399-A and 29% at Hole U1400-C (Figure 11, Table 2). Information on deformations within the cores is thus lacking in those areas. Additionally, the presence of several, thick turbidity current deposits (Table 2) also makes distinguishing deformation structures from hemipelagic beds difficult, especially as such thick sands may represent artificial suck-in during coring [*Jutzeler et al.*, 2014]. Such difficulty is mitigated when CT-scanning data occur and may reveal deformation micro-structures within some turbidity current deposits (Figure 10). Therefore, areas where deformation cannot be well distinguished correspond to 52% of core at U1399-A, and up to 33% at U1400-C (Table 2; Figure 11). Most of the missing data are located deeper than 200 meters in the Holes (Figure 11).

Correlations between the cores have been established based on amount and style of deformation (zones A, B, and C) (Figure 11). Zone A does not contain significant deformation. Hole U1399-A shows some weakly inclined beds, whereas no deformation appears in this upper zone in Hole U1400-C. The base of this zone correlates well between both sites.

Zone B represents the deformed part of each drilled Hole. It is divided into four subunits, depending of the degree of deformation (Figure 11). Subunit B1 is characterized by strong deformations intercalated with undeformed bedding. Limits of this subunit correlate very well between both Holes. Subunits B2 displays slighter deformations and is three times as long as in Hole U1400-C than in Hole U1399-A (58.5 m long and 17.5 m long, respectively). Its base corresponds to the top of a massive turbidity current deposit in Hole U1399-A (> 8 m thick) and to a transition from high to weak deformations in Hole U1400-C. Subunit B3 corresponds to the most intensely deformed zone within the entire Zone B. In Hole U1399-A, the base of B3 is located above a massive turbidity current deposit (up to 6

meters thick), while in Hole U1400-C it is characterized by indurated sediments (at 182 mbsf) with no deformation structures below the limit (Figure 12). Finally, subunit B4 displays variable deformations in Hole U1399-A, while they are stronger in Hole U1400-C. Highly inclined and thick beds (up to 18 m thick) are intercalated with undeformed layers and many voids in core recovery (Table 1, Figure 11).

Zone C corresponds to the area under the deformed section. Zones with no (U1400-C) or few deformation structures are observed (U1399-A). The upper part of Zone C is characterized by a succession of many turbidity current deposits with numerous voids in core recovery in the deepest zones of both cores (Table 1; Figure 11). This suggests a significant margin of error in our basal boundary estimation of the deformation zone. We therefore rely on seismic data to assess the basal limits at these sites (Figure 13).

In summary, Hole U1400-C is clearly more deformed than Hole U1399-A. It displays thicker and stronger deformed beds that are not observed into Hole U1399-A. This estimated total deformed thickness of stratigraphy in Hole U1399-A is 138 m thick while it is 367 m thick in Hole U1400-C (Figure 11).

5. Discussion

In this part, we first discuss how the unusual drill cores from 340 IODP Expedition constrain the nature of different seismic facies. Then, we discuss the two different processes of instabilities identified for Martinique: 1/ the subaerial instabilities (flank-collapse events generating debris avalanche deposit DAD) and 2/ the submarine instabilities (seafloor sediment failure generating the submarine landslide deposit (SLD). We especially focus on the characteristics of the submarine landslide deposit (SLD) highlighted by this study, and having implications for understanding emplacement processes. We propose a model to explain how flank-collapse events are linked to seafloor sediment failure within the evolution of Montagne Pelée volcano. Thus, implications of these emplacement processes for tsunami hazards are discussed.

5.1. Correlation between seismic facies and core observations

Previous studies of submarine landslides have typically been based on 2D or 3D seismic datasets, sometimes with short (< 10 m) sediment cores that do not penetrate fully through the landslide deposit. IODP Expedition 340 provides deep cores penetration that is rare in non-volcanic settings. This study therefore represents a valuable opportunity to compare seismic facies with core observations. Such comparison allows us to understand the amount and style of deformation and sediment lithologies that produce the different seismic facies. A key issue for such comparison is the substantial differences in resolution of the two types of data, which ranges from millimeters for the core to hundreds of meters for seismic data (Figure 13).

We observe a correlation between the upper and lower limits of the submarine landslide deposit (i.e. SLD) identified using seismic profiles and the extent of the deformation within drilled holes (Figure 13). The well-bedded seismic facies corresponds to turbidity current deposits and/or debris flow deposits, or tephra layers interbedded with hemipelagic sediments, which are flat lying and lack deformation in the cores. SLD deposit in core U1399-A is characterized by a greater degree of structure in seismic data than the more chaotic seismic facies in Hole U1400-C (Figure 13). The disturbed seismic facies in core U1399-A comprises alternations of undeformed thin beds, thicker turbidite sand layers, homogenized sandy-mud layers (debris flow deposits or localized shear zones), and zones of both weaker and stronger deformation (Figure 13A). A higher percentage of undeformed strata in the upper part of the SLD deposit in Hole U1399-A may correlate to better bedding in that part of the seismic image (Figure 13A). Chaotic seismic facies in Hole U1400 corresponds mainly to thinly-bedded hemipelagic sediments, turbidity current deposits and tephra layers that may be undeformed, weakly deformed or strongly deformed (Figure 13B). Thicker turbidite sands or homogenized sandy-mud layers are rare or absent in Hole U1400-C, A higher fraction of weakly deformed intervals near the top of SLD in Hole U1400-C corresponds to a greater degree of structure in the seismic image. Therefore, these results suggest that the type of seismic facies mainly depends on i) degree of deformation, ii) lithologic composition and iii) thickness of deformed beds. A striking feature is that the landslide deposit can contain a significant fraction (~20%) of undeformed strata, or intervals with weak deformation styles (Figure 12). Chaotic or disturbed seismic facies may therefore not always be a record of pervasive, strong deformation.

5.2. Emplacement of debris avalanches deposits (DAD), related to volcano flank-collapses events

The Montagne Pelée volcano has suffered of three flank collapse events in the southwestern direction, generating debris avalanches that flown down to the Caribbean Sea [*Deplus et al*., 2001; *Le Friant et al*., 2003a; *Boudon et al*., 2007]. The flank-collapse structures have well been identified on-land by those authors. However, our contribution underlines that only the debris avalanche deposit 3 (DAD3) associated to the more recent flank collapse event is clearly identified offshore from seismic and IODP cores data. The DAD3 has a blocky surface, and attempts to drill core through this deposit were unsuccessful [*Le Friant et al*., 2013]. Such lack of core penetration itself suggests that the DAD3 deposit has a high component of large volcanic blocks. Debris avalanche deposits 1 and 2 (DAD1 and DAD2), were not directly found offshore. The seismic data in steeper proximal areas that represent the submarine flank of the island are of poor quality and equivocal, although hyperbolic reflections could indicate the presence of some blocks (Figure 5). However, the bathymetric data show a bulge at the base of the submarine flank of the volcano, localized around the slope break (Figure 2) at the same location than DAD3. Thus, we propose that this bulge at the slope break results from the accumulation of older debris avalanche deposits (DAD1 and DAD2) related to the first and second flank-collapses of the Montagne Pelée volcano but unfortunately, we do not have any offshore drilling in this location.

5.3. Emplacement of submarine landslide deposit (SLD), related to seafloor sediment failure

The submarine flank of Montagne Pelée volcano has experienced seafloor sediment failure, generating a large submarine landslide deposit (SLD). We now focus and discuss the characteristics displayed by the SLD, from larger-scales to smaller-scales. Our underlying aim is to understand how the SLD was emplaced.

5.3.1. The SLD's geometry: internal structure and basal surface

The SLD displays a characteristic and prominent morphological front on its surface, with a difference in height of up to 35 m (Figure 5). Its origin can be related to the frontal

emergent ramp at the base of the SLD, located 7-8 km further upslope. The frontal ramp represents the location where the landslide's decollement surface ramps up from deeper to shallower stratigraphic levels (Figures 5 and 6). Movement of material across this structure would act to thicken the overlying landslide deposit in such a down-slope location [*Frey-Martinez et al*., 2005, 2006].

In addition, to this striking emergent feature in its central part, the SLD displays as well as a frontally confined distal margin. Both morphological front and frontal ramp suggest important kinetic energy during deposit emplacement [*Frey-Martinez et al*., 2006] (Figures 5B; central panel). However, the distal margin of the SLD shows interval of deformed strata in the seismic profiles that abuts against a series of undeformed and well-bedded reflectors (Figures 5B and 6B; distal panel). Such frontal confinement is the characteristic of landslides with limited and slow down-slope movement, such that the landslide mass has insufficient energy to emerge and travel along the seafloor [*Frey-Martinez et al*, 2006]. The more distal unit of the SLD displays a series of inclined compressional features, which accommodate shortening in the landslide toe region. A broadly similar frontally confined geometry has been described for volcanic island landslides offshore Montserrat in the Lesser Antilles, where many intact remnant blocks of sediments occurred offshore the island, that could be as long as 1 km and 70 m high [*Watt et al.,* 2012a]. It is presumed that one of these, included within a landslide deposit offshore the same island [i.e. Deposit 2; *Le Friant et al*., 2015] has been drilled during the Expedition IODP 340. The authors attribute this undeformed structure to deep seafloor incision and limited displacement of the landslide wherein it is comprised. Undeformed intervals also occur within drill cores U1399-A and U1400-C, suggesting that material may have experienced limited transport to keep well-preserved strata, or it was sufficiently consistent and resistant to support deformation and displacements. However, the frontally confined distal margin associated with the presence of a prominent morphological front could suggest large displacement and two phases of deformation could occur.

Core penetration by IODP drilling provides an opportunity to document the basal part of a submarine landslide deposit. Processes acting on (or near) the base of a submarine landslide can profoundly affect its emplacement process; for instance, by determining the degree of basal friction and hence velocity. The base of the SLD in Holes U1399-A and U1400-C has been constrained through seismic data, and by identifying the deepest level of deformation in the core. Figure 12 provides a detailed description of the landslide base,

showing that the landslide base at Hole U1399-A (160.5 or 174 m) may be associated with either an upward transition from massive turbidity sand to interbedded hemiplegic sediment at 160.5 m, or a thin zone of highly inclined bedding at 174 m that lies below a homogenized muddy-sand (Figure 8). In both cases, it is associated to main changes in lithology which occur elsewhere in Hole U1399-A. The deepest deformation in Hole U1400-C occurs at 390 m below seafloor (Figure 11). However, it is possible that the landslide base occurs within zones of no core recovery in the lower part of Hole U1400-C (Figure 11). The lower part of Hole U1400-C is dominated by hemipelagic mud and thinly-interbedded tephra (eruption fall-out) and thin turbidity layers. Therefore, the base of SLD is also not an unusual lithology for Hole U1400-C. Taken together, the observations at Holes U1399-A and U1400-C suggest that the basal surface of the landslide is relatively subtle, and there is no clear evidence for a single surface of unusually strong shear, which also could not be detectable in fine-grained, homogeneous sediments. Deformation appears to be distributed throughout a larger stratigraphic interval.

5.3.2. Homogenized sandy-mud layers – debris flow deposits or localized shear zones?

Intervals of homogenized muddy-sand are observed at Site U1399, although they are absent at Site U1400. They could result from pervasive mixing of pre-existing stratigraphy within localized zones of intense shear. If this is the case, such zones of intense shear were typically up to several meters in thickness, and occurred at multiple levels within the more distal part of the SLD.

However, an alternative hypothesis is that the homogenized sandy-mud intervals are submarine debris flow deposits. Both hypotheses can explain the occurrence of clasts within these layers (Figure 10), sharp upper and lower boundaries to the sandy-mud, and their homogenous sand-mud composition. In a few places both the upper and lower boundary of the sandy-mud layers appears to erode into and truncate adjacent beds, and this may favour a shear zone origin. Submarine debris flow deposits are often found to be encased in turbidity sand, whose grain size forms a continuous normally graded sequence, and whose upper part is ripple cross laminated [*Talling et al.*, 2013, 2014]. Such features of hybrid (turbidite-debrite) beds are absent at Site U1399, again favoring a shear zone origin. However, submarine debris

flows can produce thin deposits on low gradients in distal settings [*Talling et al*., 2010], and a debris flow origin cannot be precluded for the homogenized sand-mud layers.

5.3.3. *Evidence for continued high excess pore pressures in the SLD*

Excess pore pressures play a key role in triggering submarine landslides, which occur on much lower gradients that most terrestrial landslides. *Lafuerza et al*. [2014] analyzed the upper 200 m of cores at Sites U1397, U1398, U1399 and U1400 of the IODP expedition 340. They demonstrated that low hydraulic conductivity of hemipelagic sediments causes low rates of dewatering in turbidity current deposits and tephra layers, leading to excess pore fluid pressures with depth. In all cores, the upper 200 m display evidence of excess pore fluid pressure, except for site U1400 where overpressure occurs after 180 m. This has been explained by the diffusion of pore fluid from more permeable turbidity current deposits and tephra layers sandwiched between hemipelagic sediments in Hole U1400-C (Figure 9).

Also, *Hornbach et al*. [submitted] combined down-hole logging data with a rock physics model [*Hornbach and Manga*, 2014] and lithological data to assess pore pressures at Site U1399. They concluded that unusually high excess pore pressures occur at the present day in multiple sand-rich zones with SLD at this location. This conclusion was consistent with measured Vp/Vs ratios at this core site. Their work indicates that these excess pore pressures reside in thicker sand-rich intervals. Intervening mud-rich zones had very low permeabilities (10^{-16} to 10^{-19}) and acted as seals, and areas outside the SLD also lacked such elevated pore pressures. *Hornbach et al.* [submitted] used a simplified slope stability analysis to suggest that these excess pore pressures approached values needed to make the modern slope close to failure. This in turn might suggest that high excess pore pressures can persist for very long periods within the SLD, long after it initially failed. This might suggest that deformation of SLD could be continuing at the present day, or in recent times [*Hornbach et al*., submitted].

The analysis of Hornbach et al. [submitted] is consistent with our observation that multiple, post-deposition deformation zones exist within cores U1399-A and U1400-C, suggesting not only a single layer at the base of the SLD, but a series of failure prone horizons within the SLD (Figure 11). These failure prone horizons may coincide with sand layers, or boundaries between sand and mud layers, that occur in many places in these cores. It is also possible that homogenized muddy-sand layers result from previous distributed shearing at

multiple levels, and these muddy-sand layers now represent seals to pore pressure. Therefore, these layers represent multiple decollement surfaces that when they are sought, may act together to promote and enhance the deposit mobility and longer run-out distances.

However, our study does not support the view that deformation associated with the SLD has continued to near the present day [*Hornbach et al*., submitted]. Both seismic lines, core data and CAT-scan analyses show that a continuous undeformed layer of sediment drapes the SLD. The thickness of this drape above the SLD is variable, but it is typically several tens of meters thick. Assuming a reasonable average sedimentation rate of ~20 cm/ky [*Reid et al*.,] this drape suggests that deformation stopped around 100 ky before present.

5.4. Evolution of the Montagne Pelée volcano: How aerial volcano flank-collapses are linked to seafloor sediment processes?

It is likely that the SLD deposit was triggered by emplacement of one or more of the debris avalanche deposits (DAD) coming from the subaerial volcano flank-collapses. This is consistent with alignment of the submarine deposits and the horseshoe-shaped subaerial collapse scares (Figure 2). We propose that volcano flank-collapses on Montagne Pelée generate debris avalanches that enter the sea, stop at the base of the submarine flank and incise and load the seafloor sediments, to generate failure, propagation and deformation of marine sediments. Such triggering would induce a seafloor sediment failure that progressed into a submarine landslide long as many tens of kilometers in a downslope direction, from shallower-water into deeper-water.

Regarding time constraints and emplacement processes, the main question is now to understand if the SLD is linked to only one of the three subaerial flank-collapse (the first one) or if the seafloor sediment deformation of the SLD could result from successive loading of marine sediments with debris avalanche deposit (DAD) coming from the volcano. However, considering key elements such as the as 1/ the frontally emergent geometry of the SLD, implying high kinetic energy, 2/ its composition, made of highly deformed hemipelagic, turbiditic or volcanic materials, forming multiple potential decollement surfaces, 3/ the alignment of the SLD at sea with the flank-collapse structures on-land, we suggest one of the most likely scenario linking subaerial and submarine processes at Montagne Pelée (Figure 14), and propose the following model.

The first flank-collapse affecting Montagne Pelée volcano occurred around 127 ± 2 ka [*Germa et al*., 2011], generating a first horseshoe-shaped structure associated to an estimated collapse volume of 25 km^3 [*Le Friant et al*., 2003a]. The debris avalanche entered the sea, flowed over the submarine volcano slope, to stop and deposit around the slope break (i.e. slope break, Figure 2). This first – and the largest - debris avalanche deposit loaded, weakened seafloor sediment and initiated failure. Resulting submarine landslide propagates along a decollement surface, deforming in-situ alternation of hemipelagic sediments and turbidity deposits. Distributed shearing at multiple levels may have acted as potential sliding surfaces within the SLD, favoring emergence process in one or many steps. The SLD translated across the seafloor and stopped in a confined way. The resulting deposit's geometry was probably broadly corresponding to the current outline deposit, which is consistent with the preliminary age proposed by Le Friant et al., [2015] for the SLD (~115 ka). Ongoing $^{18}\delta O$ stratigraphy dating on the IODP cores will provide more precise time constraints on the development of the distal and the central parts of the SLD, and thus, on the dynamic emplacement of the submarine landslide.

The second flank-collapse event occurred following the construction of a new and voluminous edifice inside the first horseshoe-shaped structure; it generates a debris avalanche deposit (DAD2) with a volume of 13 km^3. This event occurred probably between 45 and 127 ka. DAD2 emplaced over the first one (DAD1), may have triggered the remobilization of the unconsolidated surficial sediments within the central part of the SLD, until the morphological front. This could have been also responsible of the SLD southward drifting in its southern part (Figure 2).

Finally, the new cone was destroyed again by a third flank-collapse event forming a smaller horseshoe-shaped structure with a collapse volume of 2 km^3. The age of the associated debris avalanche deposit, identified on land and offshore is also discussed and may be between 30 ka - 45 ka [*Le Friant et al*., 2015]. As the previous event, the debris avalanche deposit DAD3 related to this last event, that is clearly identified on the submarine flank may have locally remobilized sediments within the SLD, by exerting a normal stress that supplied the deformation process.

5.5. Implications for tsunami generation

Both the composition and hence source of landslide material, and how the landslide was emplaced have major implications for the magnitude of tsunami that a submarine landslide generates [*Masson et al*., 2006; *Ward*, 2001; *Ward and Day*, 2001; *Watt et al*., 2012 b, 2014]. The model presented in this study implies that a large submarine landslide (300 km^3) occurred offshore Martinique, associated to the entering at sea of the one of the largest debris avalanche recognized in the Montagne Pelée history (25 km^3). A landslide that comprises seafloor sediment will produce a much smaller tsunami than a landslide that originates from either subaerial or submerged parts of the volcanic edifice [see *Watt et al*., 2012a]. A frontally confined landslide geometry also suggests limited lateral displacement of landslide material, and relatively slow landslide velocities [*Frey-Martinez et al*., 2006; *Watt et al*., 2012a,b]. These two factors will therefore reduce the tsunami hazard from these submarine landslides offshore Martinique without decreasing the effects of a tsunami generated by the entry into the sea of a large mass of material as it is the case for debris avalanches.

6. Conclusions

This study presents results from the first scientific drilling of large submarine landslide deposits offshore from volcanic islands, completed by IODP Expedition 340 offshore Martinique. It combines new seismic reflection data with two IODP drill sites (U1399 and U1400) data to propose a new model linking subaerial and submarine instability processes in Martinique. Debris avalanche deposits generated by Montagne Pelée volcano flank-collapse events, enter the sea and load the marine sediment triggering submarine landslides and the formation of SLD. Our study reveal how deep drilling data combined with seismic data are crucial to avoid misunderstandings and underestimations of submarine landslide processes offshore volcanic islands. This new interpretation has implications for similar volcanic island contexts, also prone to volcano flank-collapse processes, (e.g. Hawaii, Canary, La Réunion, Stromboli….) where drilling data are not available through landslide deposits.

Acknowledgements

This study was funded by INSU, ANR CARIB. The authors thank the drillers and all R/V JOIDES Resolution staff for their collaboration and efficient work on board during the IODP Expedition 340. The authors are grateful to Christine Deplus, Nathalie Feuillet who were PI of the oceanographic cruises AGUADOMAR, CARAVAL and GWADASEIS cruises. We also acknowledge John Firth (IODP's Gulf Coast Repository), and Wade Friedrieck and its team (College of Veterinary Medicine, TAMU) for their help and dedication during CT-Scan acquisition. Data from the IODP Expedition 340 can be obtained through the expedition's implementing organization USIO (http://iodp.tamu.edu/database).

References

Boespflug, X., B. F. N. Long, and S. Occhietti (1995), CAT-scan in marine stratigraphy: A quantitative approach. Marine Geology, 122, 281–301.

Boudon, G., A. Le Friant, B. Villemant, and J.-P. Viode (2005), Martinique, in Volcanic Atlas of the Lesser Antilles, edited by J. M. Lindsay et al., pp. 65–102, Seismic Res. Unit, Univ. of the West Indies, Trinidad and Tobago.

Boudon, G., A. Le Friant, J.-C. Komorowski, C. Deplus, and M. P. Semet (2007), Volcano flank instability in the Lesser Antilles Arc: Diversity of scale, processes, and temporal recurrence. J. Geophys. Res., 112, B08205, doi:10.1029/2006JB004674.

Boudon, G., B. Villemant, A. Le Friant, M. Paterne, and E. Cortijo (2013), Role of large flank-collapse events on magma evolution of volcanoes. Insights from the Lesser Antilles Arc, J. Volcanol. Geotherm. Res, 263, 224–237, doi:10.1016/j.jvolgeores.2013.03.009.

Bouysse, P., D. Westercamp, and P. Andreieff (1990), The Lesser Antilles Island Arc, Proc. Ocean Drill. Program Sci. Results, 110, 29– 44.

Bull, S., J. Cartwright and M. Huuse (2009), A review of kinematic indicators from mass transport complexes using 3D seismic data. Marine and Petroleum Geology 26 (7), 1132–1151.

Carracedo, J. C. (1999), Growth, structure, instability and collapse of Canarian volcanoes and comparisons with Hawaiian volcanoes. Journal of volcanology and Geothermal Research, 94 : 1-19.

Cassidy, M., S.F.L. Watt, M.R. Palmer, J. Trofimovs, W. Symons, S. Maclare and, A. Stinton (2014), Construction of volcanic records from marine sediment cores: A review and case study (Montserrat, West Indies)'. Earth Science Reviews. 138, 137-155 pp DOI: 10.1016/j.earscirev.2014.08.008

Cohen, J. K., and J.J.W. Stockwell (1996), CWP/SU: Seismic Unix release 28: A free package for seismic research and processing, Cent. for Wave Phenomena, Colo. Sch. of Mines, Golden.

Crandell, D. R. (1989), Gigantic debris avalanche of Pleistocene age from ancestral Mount Shasta volcano, California, and debris-avalanche hazard zonation, U. S. Geol. Surv. Bull., 1861, 32 pp.

Delcamp, A., B. Van Wyk de Vries, and M. James (2008), The influence of edifice slope and substrata on volcano spreading, J. Volcanol. Geotherm.Res., 177(4), 925–943.

Deplus, C., A. Le Friant, G. Boudon, J.-C. Komorowski, B. Villemant, C. Harford, J. Ségoufin, and J.-L. Cheminée (2001), Submarine evidence for large-scale debris avalanches in the Lesser Antilles Arc. Earth Planet. Sci. Lett., 192, 145– 157.

Deplus, C., A. Le Friant, G. Boudon, J.-C. Komorowski, S. Sparks, and C. Harford (2002), Numerous DADs off the southern part of Monserrat revealed by recent oceanographic cruises. Paper presented at International Congress on Montagne Pelée 1902– 2002, IPGP-INSU-IAVCEI, Martinique Island, 12– 16 May.

Duliu, O. (1999), Computer axial tomography in geosciences: An overview. Earth Science Reviews, 48, 265–281.

Frey-Martinez, J., J. Cartwright and B. Hall (2005), 3D seismic interpretation of slump complexes: examples from the continental margin of Israel. Basin Research 17, 83–108.

Frey-Martinez, J., J. Cartwright and D. James (2006), Frontally confined versus frontally emergent submarine landslides: a 3D seismic characterization. Marine and Petroleum Geology 23 (5), 585–604.

Gee, M.J.R., R.L. Gawthorpe and J.S. Friedmann (2005). Giant striations at the base of a submarine landslide. Marine Geology 214, 287–294.

Germa, A., X. Quidelleur, P. Lahitte., S. Labanieh and C. Chauvel (2011), The K–Ar Cassignol–Gillot technique applied to western Martinique lavas: a record of the evolution of the recent Lesser Antilles island arc activity from 2 Ma to Mount Pel.e volcanism. Quaternary Geochronology 6, 341–355.

Guyard, H., P. Francus, G. St-Onge, S. Hausmann and R. Pienitz (2014), Microfacies and microstructures of subglacial and deglacial sediments from the Pingualuit Crater Lake (Ungava Peninsula, Canada). Canadian Journal of Earth Sciences 51 (12), 1084-1096.

Harbitz, C.B., S. Glimsdal, S. Bazin., N. Zamora, H.C. Smebye, F. Løvholt, H. Bungum, P. Gauer and O. Kjekstad (2012), Tsunami hazard in the Caribbean: Regional exposure derived from credible worst case scenarios. Continental Shelf Research, 38, 1–23.

Hornbach, M.J., and M. Manga (2014), The ability of rock physics models to infer marine in situ pore pressure, Geochem. Geophy. Geosyst., 15, 4769-4780, doi:10.1002/2014GC005442.

Iverson, R. M. (1997), The physics of debris flows, Rev. Geophys., 35, 245–296.

Jutzeler, M., J.D.L. White, P.J. Talling, M. McCanta, S. Morgan, A. Le Friant and Ozamu Ishizuka (2014), Methods for identifying coring disturbance in IODP piston cores and implications for volcanic events offshore Montserrat and deep sea record of Missoula mega-floods. G-cubed. v. 15, p. 3572-3590

Labazuy, P. (1996), Recurrent landslides events on the submarine flank of Piton de la Fournaise volcano (Reunion Island), in Volcano Instability on the Earth and Other Planets, Geol. Soc. Spec. Publ., vol. 110, edited by W. J. McGuire, A. P. Jones and J. Neuberg, pp. 295–306,London, U. K., doi: 10.1144/GSL.SP.1996.110.01.23.

Lacroix, A. (1904), La Montagne Pelée et ses Eruptions, 662 pp., Masson et Cie, Paris.

Lafuerza S., A. Le Friant, M. Manga, G. Boudon, B. Villemant, N. Stroncik, B. Voight, M. Hornbach, O. Ishizuka and the Expedition 340 Scientific Party (2014), Geomechanical characterizations of submarine volcano flank sediments, Martinique, Lesser Antilles Arc, in Sumarine Mass Movements and Consequences, Adv. Nat. Technol. Hazards Res., edited by S. Krastel et al., p. 37, Springer, Switzerland, doi: 10.1007/978-3-319-00972-8_7.

Lebas, E., A. Le Friant, G. Boudon, S. Watt, P. Talling, N. Feuillet, C. Deplus, C. Berndt, and M. Vardy (2011), Multiple widespread landslides during the long-term evolution of a volcanic island: Insights from high-resolution seismic data, Montserrat Lesser Antilles. Geochem. Geophys. Geosyst., 12, Q05006, doi:10.1029/2010GC003451.

Le Friant, A., G. Boudon, C. Deplus, and B. Villemant (2003a), Large-scale flank collapse events during the activity of Montagne Pelée, Martinique, Lesser Antilles, J. Geophys. Res., 108(B1), 2055, doi:10.1029/2001JB001624.

Le Friant, A., O. Ishizuka, N. A. Stroncik, and the Expedition 340 Scientists (2013), Proceedings of Integrated Ocean Drilling Program, 340, Integrated Ocean Drill. Program Manage. Int. Inc., Tokyo, doi:10.2204/iodp.proc.340.2013.

Le Friant, A., et al. (2015), Submarine record of volcanic island construction and collapse in

the Lesser Antilles arc: First scientific drilling of submarine volcanic island landslides by IODP Expedition 340, Geochem. Geophys. Geosyst., 16, doi:10.1002/2014GC005652.

Masson, D. G., A. B. Watts, M. J. R. Gee, R. Urgeles, N. C. Mitchell, T. P. Le Bas and M. Canals (2002), Slope failures on the flanks of the western Canary Islands, Earth Sci. Rev., 57, 1–35.

Masson, D.G., C.B. Harbitz, R.B. Wynn, G. Pedersen and F. Løvholt (2006), Submarine landslides: processes, triggers and hazard prediction. Philosophical Transactions of the Royal Society A 364, 2009–2039.

Martin-Kaye, P. H. A. (1969), A summary of the geology of the Lesser Antilles, Overseas Geol. Miner. Res., 10(2), 172– 206.

McGuire, W. J. (1996), Volcano instability: a review of contemporary themes, in Volcano Instability on the Earth and Other Planets, Geol. Soc. Spec. Publ., vol. 110, edited by W. J. McGuire et al., pp. 1–23, doi:10.1144/GSL.SP.1996.110.01.01.

Milliman, J. D. and J.P.M. Syvitski (1992), Geomorphic tectonic controls of sediment discharge to the ocean – the importance of small mountain rivers. J. Geol. 100, 525–544.

Moernaut, J. and M. De Batist (2011), Frontal emplacement and mobility of sublacustrine landslides: results from morphometric and seismostratigraphic analysis. Marine Geology 285 (1–4), 29–45.

Moore, J. G., D. A. Clague, R. T. Holcomb, P. W. Lipman, W. R. Normark, and M. E. Torresan (1989), Prodigious submarine landslides on the Hawaiian ridge, J. Geophys. Res., 94, 17,465–17,484.

Moore, J. G., W. R. Normark, and R. T. Holcomb (1994), Giant Hawaiian landslides, Annu. Rev. Earth Planet. Sci., 22, 119– 144, 1994.

Oehler, J. F., J. F. Lenat, and P. Labazuy (2008), Growth and collapse of the Reunion Island volcanoes, Bull. Volcanol., 70, 717–742, doi: 10.1007/s00445-007-0163-0.

Reid, R. P., S. N. Carey, and D. R. Ross (1996), Late Quaternary sedimentation in the Lesser Antilles island arc, Geol. Soc. Am. Bull., 108(1), 78–100.

Schnellmann, M., F.S. Anselmetti, D. Giardini and J.A. McKenzie (2005), Mass movement induced fold-and-thrust belt structures in unconsolidated sediments in Lake Lucerne (Switzerland). Sedimentology 52 (2), 271–289.

Siebert, L. (1984), Large volcanic debris avalanches: Characteristics of source areas, deposits, and associated eruptions, J. Volcanol. Geotherm. Res., 22, 163– 197.

Smith, W. H. F., and D. T. Sandwell (1997), Global sea floor topography from satellite altimetry and ship depth soundings, Science, 227, 1956–1962.

St-Onge, G., E. Chapron, H. Guyard, A. Rochon, P. Lajeunesse, D. Scott, J. Locat, J. S. Stoner and C. Hillaire-Marcel (2008), High-resolution physical and magnetic properties of rapidly deposited layers associated with landslides, earthquakes and floods. In : J. Locat et al. (Eds.) : Comptes rendus de la 4e Conférence canadienne sur les géorisques : des causes à la gestion. Laval University Press, Quebec, 219-228.

Talling, P.J., R.B. Wynn, R. Rixon, D. Schmidt, E. Sumner and L.A. Amy (2010), How did submarine flows transport boulder sized mud intra-clasts to the fringes of the Mississippi Fan? Journal of Sedimentary Research, v. 80, p. 829-851.

Talling, P. J., G. Malgesini, E.J. Summer, L.A. Amy, F. Felletti, G. Blackboum, C. Nutt, C. Wilcox, I. C. Harding, and S. Akbari (2012), Planform geometry, stacking pattern, and extrabasinal origin of low strength and intermediate strength cohesive debris flow deposits in the Marnoso-arenacea Formation, Italy, Geosphere, 8(6), 1207–1230, doi:10.1130/GES00734.1.

Talling, P.J., E.J. Sumner, D.G. Masson, and G. Malgesini (2012), Subaqueous sediment density flows: depositional processes and deposit types. *Sedimentology*, v. 59, p. 1937-2003.

Talling, P.J. (2013), Hybrid submarine flows comprising turbidity current and cohesive debris flow: Deposits, theoretical and experimental analyses, and generalised models. *Geosphere*, 9, 460-488.

Talling, P.J. (2014), On the triggers, resulting flow types and frequencies of subaqueous sediment density flows in different settings. Marine Geology, 352, 155-182. (doi:10.1016/j.margeo.2014.02.006).

Trofimovs, J., P. J. Talling, J. K. Fisher, R. S. J. Sparks, S. F. L. Watt, M. B. Hart, C. W. Smart, A. Le Friant, M. Cassidy, S. G. Moreton, and M. J. Leng (2013), Timing, origin and emplacement dynamics of mass flows offshore of SE Montserrat in the last 110 ka: Implications for landslide and tsunamis hazards, eruption history, and volcanic island evolution, Geochem, Geophys, Geosyst., 14, doi:10.1002/ggge.20052.

Wall-Palmer, D., et al. (2014), Late Pleistocene stratigraphy of IODP Site U1396 and compiled chronology offshore of south and south west Montserrat, Lesser Antilles, Geochem. Geophys. Geosyst., 15, doi:10.1002/2014GC005402.

Ward, S. N. (2001), Landslide tsunami, J. Geophys. Res., 106, 11,201–11,215.

Ward, S. N. and S. J. Day (2001), Cumbre Vieja volcano–potential collapse and tsunami at La Palma, Canary Islands, Geophys. Res. Lett., 28, 3397–3400.

Watt, S.F.L., P. J. Talling, M. E. Vardy, V. Heller, V. Hühnerbach, M. Urlaub, S. Sarkar, D.G. Masson, T. J. Henstock, T. A. Minshull, M. Paulatto, A. Le Friant, E. Lebas, C. Berndt, G. J. Crutchley, J. Karstens, A. J. Stinton and F. Maeno (2012a), Combinations of volcanic-flank and seafloor-sediment failure offshore Montserrat, and their implications for tsunami generation. Earth and Planetary Science Letters 319–320, 228–240.

Watt, S.F.L., P.J. Talling, M.E. Vardy, D.G. Masson, T.J. Henstock, V. Huhnerbach, T.A. Minshull, M. Urlaub, E. Lebas, A. Le Friant, and others. (2012b), Widespread and progressive seafloor-sediment failure following volcanic debris avalanche emplacement: Landslide dynamics and timing offshore Montserrat, Lesser Antilles. Marine Geology 323–325:69–94

Watt, S.F.L., P.J. Talling and J.E. Hunt (2014), New insights into the emplacement dynamics of volcanic-island landslides. Oceanography, v. 27, p. 46-57.

Wadge, G. (1985), Morne Patates volcano, southern Dominica, Lesser Antilles, Geol. Mag., 122(3), 253–260.

FIGURES CAPTIONS

FIGURE 1: Geodynamic setting of the Lesser Antilles Arc. Predicted bathymetry from Smith and Sandwell (1997). Isobaths are 500 m with 2000 m (bold isobaths). The volcanic islands (inner arc) and the coral reef platforms (outer arc) are illustrated in dark in dark gray, respectively.

FIGURE 2: Bathymetric map (from AGUADOMAR cruise, 1999 and CARAVAL cruise, 2002) showing an area southwest of Martinique, and terrestrial digital elevation model (from IGN), showing previous extents of deposits and on-land horseshoe-shaped structures [*Le Friant et al*., 2003a, 2015]. New landslide deposits extents inferred from AGUADOMAR, CARAVAL and GWADASEIS seismic data are illustrated using black lines.

FIGURE 3: Bathymetric map (from AGUADOMAR cruise, 1999 and CARAVAL cruise, 2002) offshore Martinique and terrestrial digital elevation model (from IGN). Also shown is the 2D seismic coverage based on three different datasets obtained offshore Martinique [*Deplus et al*., 2001*; Le Friant et al*., 2003a], as well as seismic lines used in this study (thick red and blue lines). Also illustrated are the sites drilled during IODP Expedition 340 in 2012. This study focuses on Sites U1399 and U1400 drilling sites (yellow dotes). Rectangles on line sections indicate the proximal, central, and distal units detailed in Figures 5 and 6.

FIGURE 4: Line 16 – CARAVAL cruise. Seismic facies characterizing the SLD . a) Well-bedded seismic facies surrounding the landslide deposit, b) Chaotic seismic facies located at the center and the ending part of the SLD, c) Disturbed seismic facies observed between the distal and final part. d) Detailed image showing the morphological front area. Image shows a continuous basal reflector. e) Chaotic-to-transparent seismic facies located at the center and the ending part of the SLD deposit.

FIGURE 5: Line 16 – CARAVAL cruise. A) Seismic profile across the SLD and associated line drawing. B) Detailed images of the proximal (upper panel), central (middle panel) and distal (lower panel) units. Associated line drawings (right panels) display the structural features along the deposit.

FIGURE 6: Line 17 – CARAVAL cruise. A) Seismic profile across the SLD and associated line drawing. Also illustrated is the younger DAD3 deposit in the proximal unit. B) Zooms on the proximal (upper panel), central (middle panel) and distal (lower panel) units. Associated line drawings (right panels) display the structural features along the deposit.

FIGURE 7: P-wave velocities measurements (m/s) in Hole U1399-A, and in Hole U1400-C, from IODP Expedition 340.

FIGURE 8: Simplified lithology and physical properties on core measurements in Hole U1399-A (bulk density, magnetic susceptibility and NGR total).

FIGURE 9: Lithostratigraphic correlations between holes of Sites U1399 and U1400. Seven units are identified in Hole U1399-A, while five units are identified in hole U1400-C (see text for details). Section boundaries are represented on the right hand side of each log.

FIGURE 10: Photographs and corresponding CT-scans of deformation features observed within U1399-A (figures 1, 2 and 6) and U1400-B (figures 3, 4, 5, 7 and 8) core sections. Brittle deformation: micro-faults (depths figure 1: 26.85m, figure 2: 45,25m). Ductile deformation: folds, convolutes, inclined banding (depths figure 3: 86,75m, figure 4: 64,95m, figure 5: 59,65m). Polyphase deformation: mixing (depth figure 6: 95,55m), and mud clasts (depth figure 8: 92,75m). Deformation micro-structures within turbidity current deposits, only discernible on CT-scans (depth figure 8: 95,55).

FIGURE 11: Correlation between Holes U1399-A and U1400-C based on deformation intensity. Area A and C represent the undeformed intervals above and below the highly deformed Area B, respectively. In Hole U1400-C, Area B is almost three times as thick as Area B in Hole U1399-A, and is also characterized by stronger deformations than in Hole U1399-A. Pore pressure ratio (λ^*) versus depth at Site U1399 is also shown [modified from *Hornbach et al*., submitted]. A value of zero indicates hydrostatic fluid pressure, whilst a value of 1 indicates lithostatic fluid pressure. Gray lines indicate model-predicted pore pressure with depth using the minimum end-member rock physics-model to match in-situ velocities. The black line corresponds to the minimum expected λ^* value necessary to trigger failure in clay-rich sediments [from *Hornbach et al*., submitted].

FIGURE 12: (A) Illustration of the base of the SLD between 170 mbsf and 154 mbsf in Hole U1399-A. Hemipelagic sediment packages surrounding a 6 m thick turbidity current deposit. The top of this package marks the base of the deformation zone estimated at 161 mbsf. (B)

Illustration of the base of the SLD between 400 and 381 mbsf in Hole U1400-C. Highly indurated hemipelagic sediments alternating with numerous tephra layers. The base of deformation is localised among these alternating layers at 391 mbsf. The basal surface of the SLD is characterized by turbidity current deposits and/or tephra layers intercalated within hemipelagic sediments, probably acting as low shear strength level and resulting in the basal decollement surface (see text for details).

FIGURE 13: Correlation using both seismic and drilling data for (A) Hole U1399-A and (B) Hole U1400-C based on deformation zone limits. Both datasets are well correlated despite their large resolution differences. Please refer to legends in figures 8 and 10 for key.

FIGURE 14: Conceptual model of the relation between aerial instability processes (i.e. volcano flank-collapse events) and submarine instability processes (i.e. seafloor sediment failure). The first debris avalanche deposit weakened and initiated seafloor-sediment failure, that resulted in a submarine landslide propagation Successive debris avalanches deposits remobilized the unconsolidated surficial sediments within the proximal part of the submarine landslide deposit (SLD)

SUPPLEMENTARY MATERIAL

FIGURE S1: Line 17 – CARAVAL. Three distinct seismic facies characterize the SLD. a) Well-bedded seismic facies surrounding the landslide deposit, b) and e) Chaotic and chaotic-to-transparent seismic facies located at the center and the ending part of the SLD, c) Disturbed seismic facies observed between the distal and final part. d) Zoom on the morphological front area, showing no reflector and no sediment package allowing to distinguish the two units as previously suggested ("D1 and D2", Le Friant et al., 2003a) that are now interpreted as one large submarine landslide deposit (SLD).

Appendix : IODP SCIENCE PARTY

Nicole A. Stroncik□Expedition Project Manager/Staff Scientist

Integrated Ocean Drilling Program

Texas A&M University

1000 Discovery Drive

College Station TX 77845-9547

USA

nstroncik@gfz-potsdam.de

Angela L. Slagle□Logging Staff Scientist

Borehole Research Group

Lamont-Doherty Earth Observatory

of Columbia University

PO Box 1000, 61 Route 9W

Palisades NY 10964

USA

aslagle@ldeo.columbia.edu

Sally Morgan□Logging Staff Scientist

Borehole Research Group

Department of Geology

University of Leicester

University Road

Leicester LE1 7RH

United Kingdom

sm509@leicester.ac.uk

Tatsuya Adachi□Physical Properties/Downhole Measurements Specialist

Department of Earth and Environmental Science

Yamagata University

1-1-18 Yakushi-machi

Yamagata 990-0053

Japan

s11e501m@st.yamagata-u.ac.jp

Mohammed Aljahdali□Micropaleontologist (nannofossils)

Department of Earth, Ocean and Atmospheric Sciences

Florida State University

108 Carraway Building

Tallahassee FL 32306-0001

USA

ma10u@my.fsu.edu

Christoph Breitkreuz□Physical Properties/Downhole Measurements Specialist

Physical Volcanology and Sedimentology

Institut für Geologie und Paläontologie

Technische Universität Bergakademie Freiberg

Bernhard-von-Cotta Strasse 2

09599 Freiberg

Germany

cbreit@geo.tu-freiberg.de

Daisuke Endo□Sedimentologist/Volcanologist,

A203, Earth Evolution Sciences

University of Tsukuba

1-1-1 Tennodai

Tsukuba

Ibaraki 305-8572

Japan

endora@geol.tsukuba.ac.jp

Andrew J. Fraass□Micropaleontologist (foraminifers)

Department of Geosciences

University of Massachusetts

611 North Pleasant Street

Amherst MA 01003

USA

afraass@geo.umass.edu

Akihiko Fujinawa□Sedimentologist/Volcanologist

Department of Earth Sciences

Ibaraki University

2-1-1 Bunkyo

Mito

Ibaraki 310-8512

Japan

fujinawa@mx.ibaraki.ac.jp

Robert G. Hatfield□Paleomagnetist

College of Oceanic and Atmospheric Sciences

Oregon State University

104 COAS Administration Building

Corvalis OR 97331-5503

USA

rhatfield@coas.oregonstate.edu

Martin Jutzeler□Physical Properties Specialist

Geology Department

University of Otago

PO Box 56

Dunedin 9054

New Zealand

jutzeler@gmail.com

Kyoko S. Kataoka□Sedimentologist/Volcanologist

Research Institute for Natural Hazards and Disaster Recovery

Niigata University

2-cho 8050 Ikarashi

Nishi-ku

Niigata 950-2181

Japan

kataoka@gs.niigata-u.ac.jp

Fukashi Maeno□Sedimentologist/Volcanologist

Earthquake Research Institute

University of Tokyo

1-1-1 Yayoi

Bunkyo-ku

Tokyo 113-0032

Japan

fmaeno@eri.u-tokyo.ac.jp

Michael Manga□Physical Properties/Downhole Measurements Specialist

Department of Earth and Planetary Science

University of California, Berkeley

307 McCone Hall

Berkeley CA 94720

USA

manga@seismo.berkeley.edu

Michael Martinez-Colon□Micropaleontologist (foraminifers)

College of Marine Science

University of South Florida, St. Petersburg

140 7th Avenue South

St. Petersburg FL 33701

USA

mmartin8@mail.usf.edu

Molly C. McCanta□Sedimentologist/Volcanologist

Department of Geology

Tufts University

2 North Hill Road

Lane Hall

Medford MA 02155

USA

mccanta@tuffts.edu

James McManus□Inorganic Geochemist

College of Earth, Ocean, and Atmospheric Sciences

Oregon State University

104 CEOAS Administration Building

Corvalis OR 97331-5503

USA

mcmanus@coas.oregonstate.edu

Martin R. Palmer□Inorganic Geochemist

School of Ocean and Earth Science

National Oceanography Centre

University of Southampton

European Way

Southampton SO14 3ZH

United Kingdom

pmrp@noc.soton.ac.uk

Takeshi Saito□Paleomagnetist

International Young Researchers

Empowerment Center

Shinshu University

3-1-1 Asahi

Matsumoto 390-8621

Japan

Present address (19 June 2014):

Department of Geology

Faculty of Science

Shinshu University

3-1-1 Asahi

Matsumoto 390-8621

Japan

saito@shinshu-u.ac.jp

Adam Stinton□Sedimentologist/Observer

Montserrat Volcano Observatory

PO Box 318

Flemmings

Montserrat

West Indies

adam@mvo.ms

Konduri S.V. Subramanyam□Inorganic Geochemist

Geochemistry Division

National Geophysical Research Institute (NGRI)

Uppal Road

Hyderabad 500 007

India

konduri2003@yahoo.com

Yoshihiko Tamura (Tabata)□Sedimentologist/Volcanologist

Institute for Research on Earth Evolution (IFREE)

Japan Agency for Marine-Earth Science and Technology

2-15 Natsushima-cho

Yokosuka 237-0061

Japan

tamuray@jamstec.go.jp

Benoît Villemant□Inorganic Geochemist

Université P&M Curie

UPMC-CNRS UMR 7193 IsTeP

T46-00 E3, Case Courier 109

4 Place Jussieu

75005 Paris

France

benoit.villemant@upmc.fr

Deborah Wall-Palmer□Micropaleontologist (foraminifers)

School of Earth, Ocean and Environmental Sciences

Fitzroy Building, Room 118

Plymouth University

Drake Circus

Plymouth PL4 8AA

United Kingdom

deborah.wall-palmer@plymouth.ac.uk

Fei Wang□Sedimentologist/Volcanologist

Institut of Geology and Geophysics

Chinese Academy of Sciences

19 Bei-Tu-Cheng-Xi Road

Chao Yang District

100029, Beijing

People's Republic of China

wangfei@mail.iggcas.ac.cn

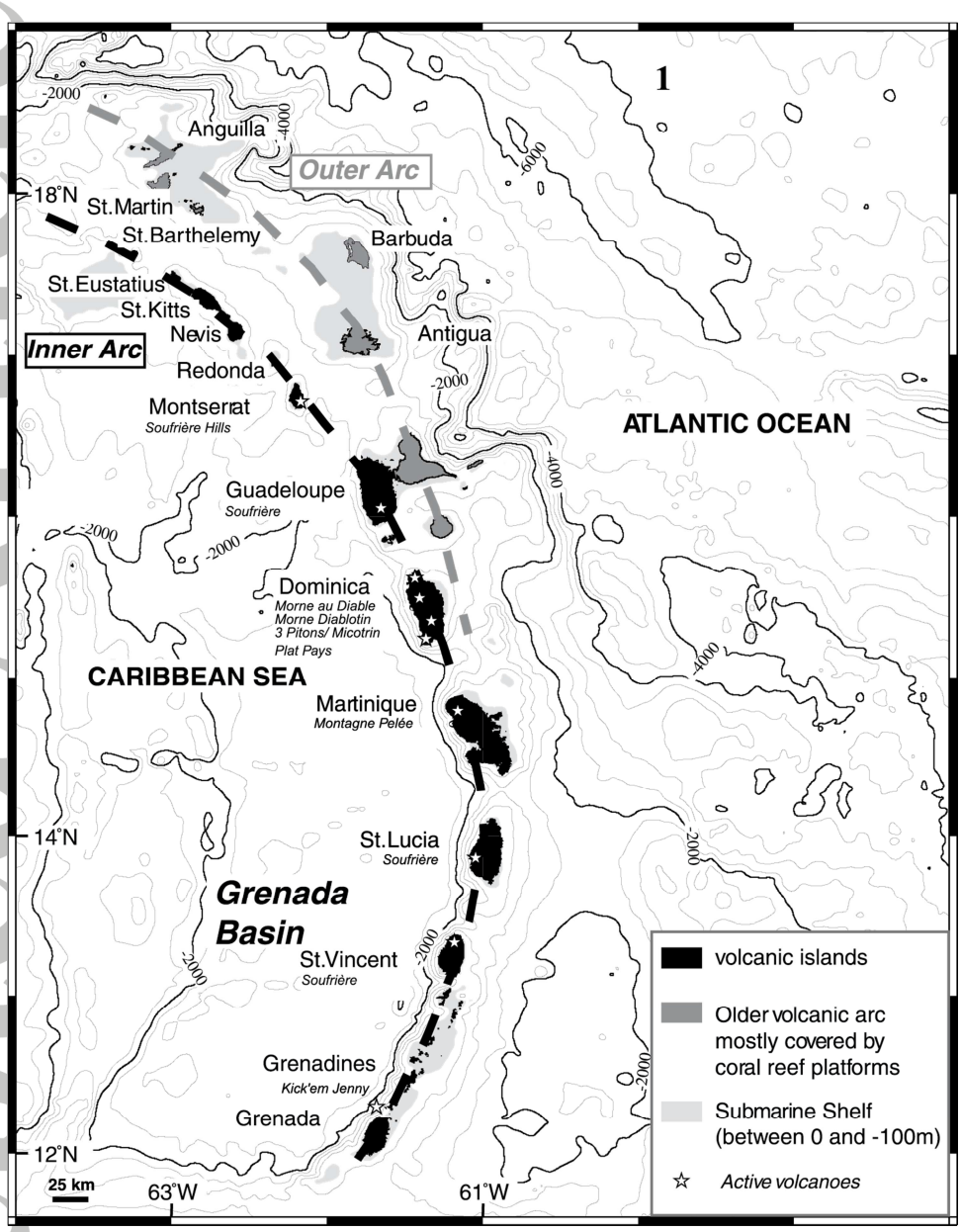

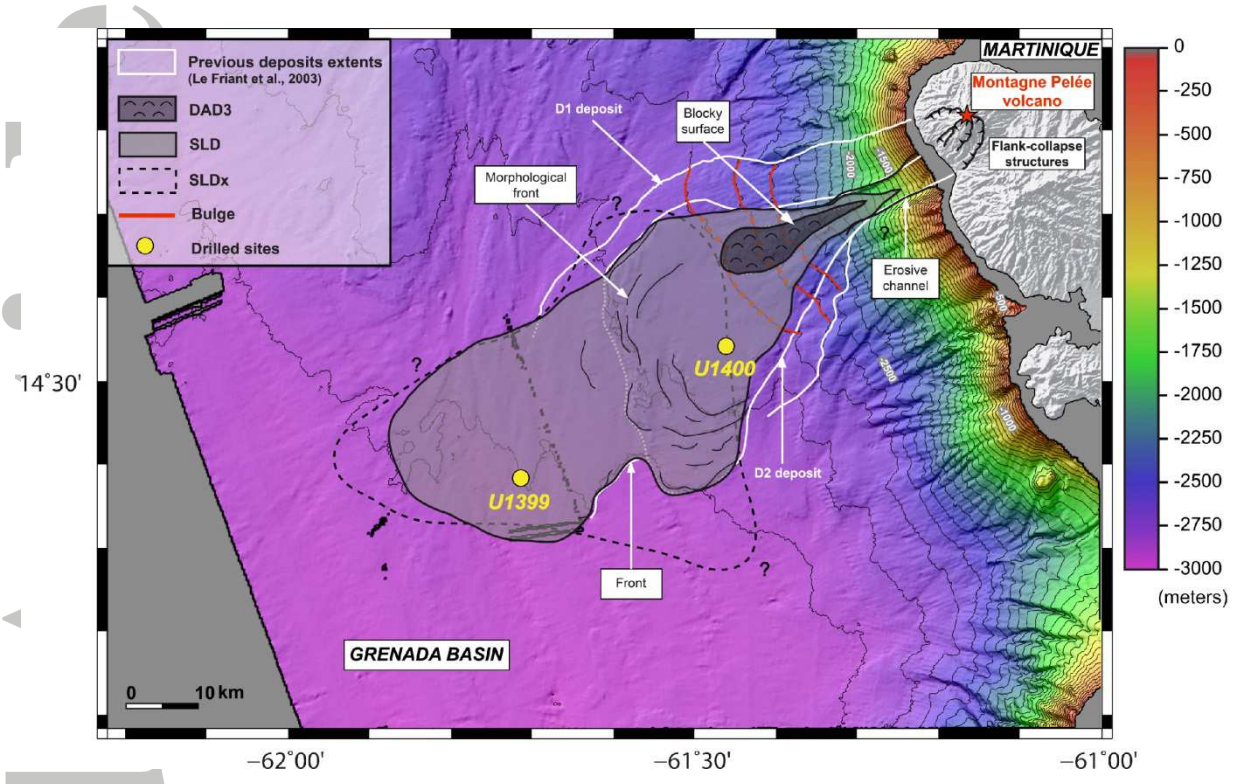

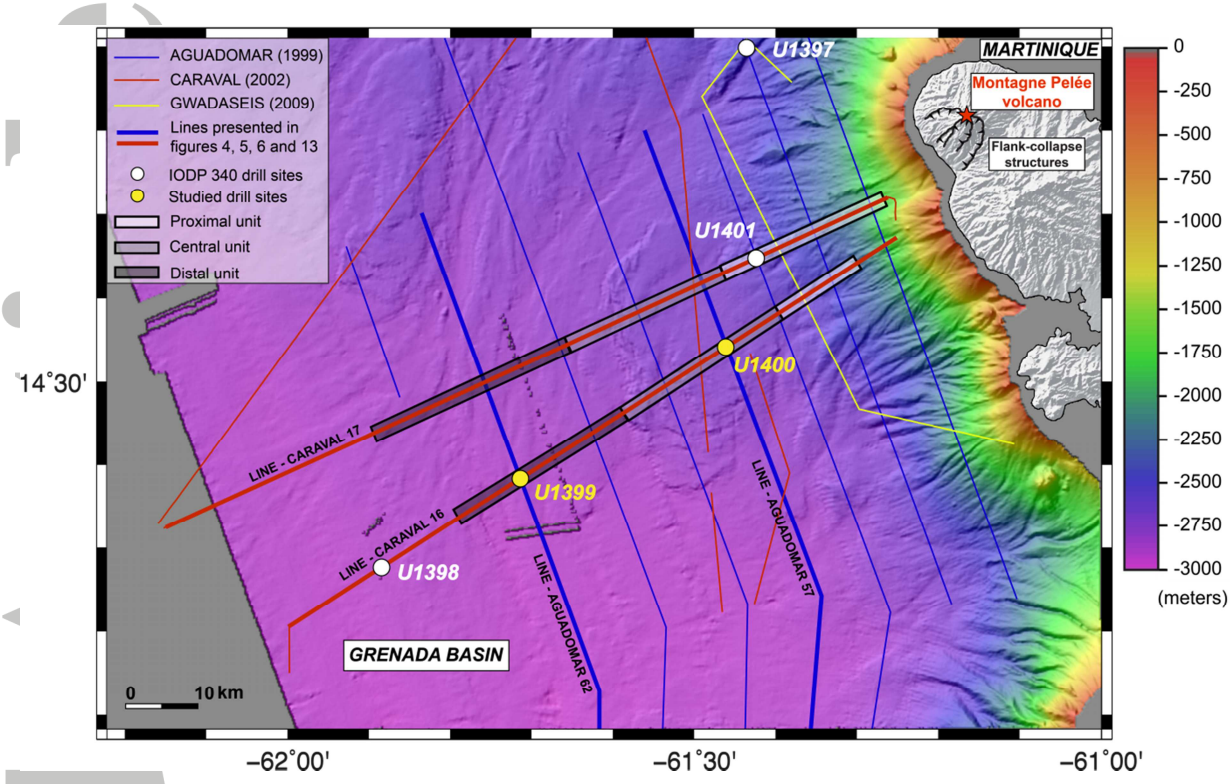

Table 1. Coring summary of U1399 and U1400 drill sites (modified from Le Friant et al. 2015)

Hole	Latitude	Longitude	Water depth (mbsl)	Penetration (mbsf)	Recovered Length (m)	Core Recovery (%)	Advanced Piston cores	Distance from the coast (km)
U1399-A	14.23,2419 N	61.42,6833 W	2900.8	274.7	219.88	80	36	
U1399-B	14.23,3639 N	61.42,5380 W	2900.2	183	183.04	10	27	
U1399-C	14.23,2593 N	61.42,6665 W	2900.8	240	**0**			63
U1400-A	14.32,5831 N	61.27,5492 W	2744.4	51.3	51.8	10	9	
U1400-B	14.32,2023 N	61.27,4065 W	2743	212.5	215.19	10	28	
U1400-C	14.32,1935 N	61.27,4028 W	2743	436	304.49	72	49	37

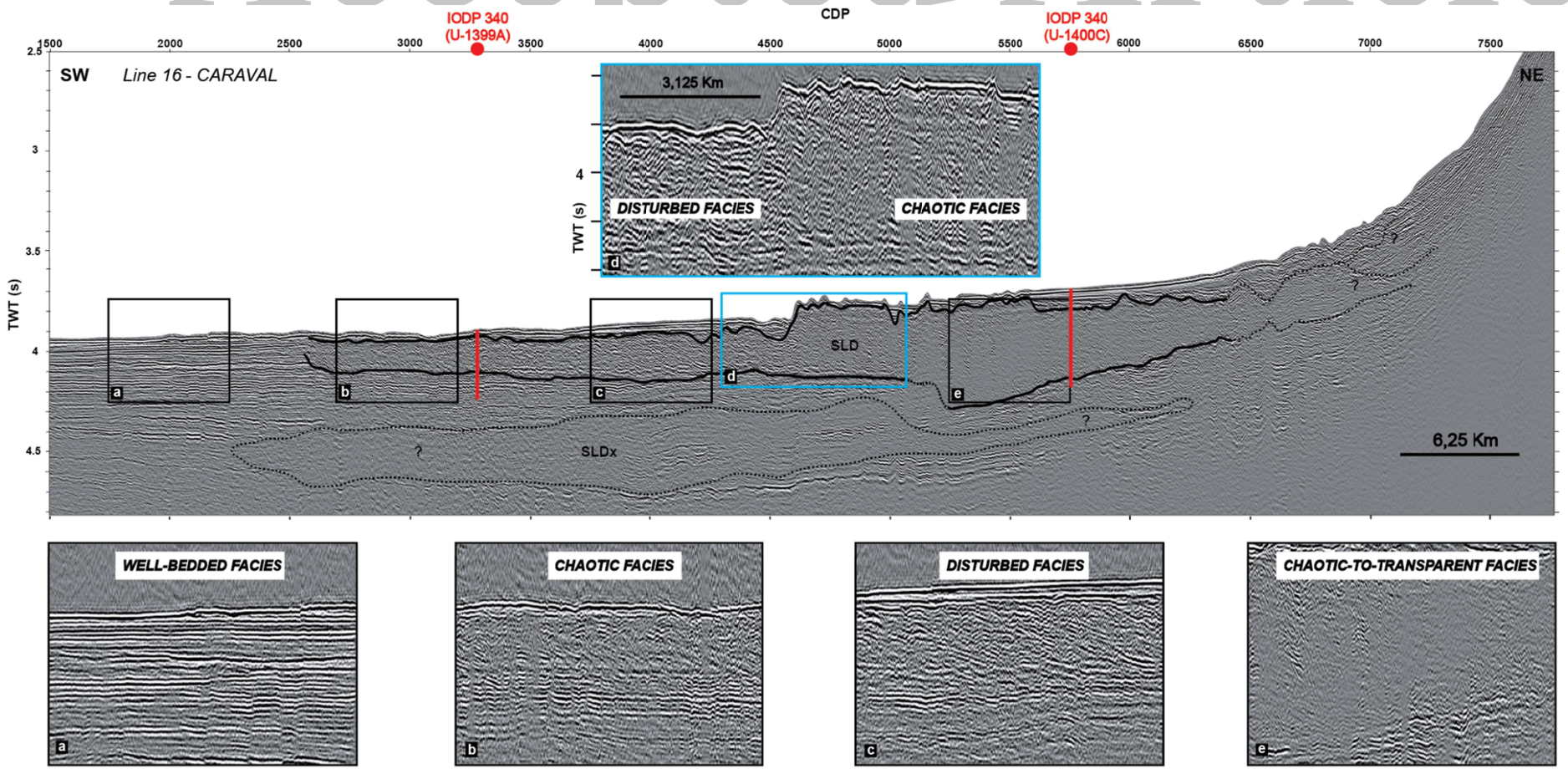

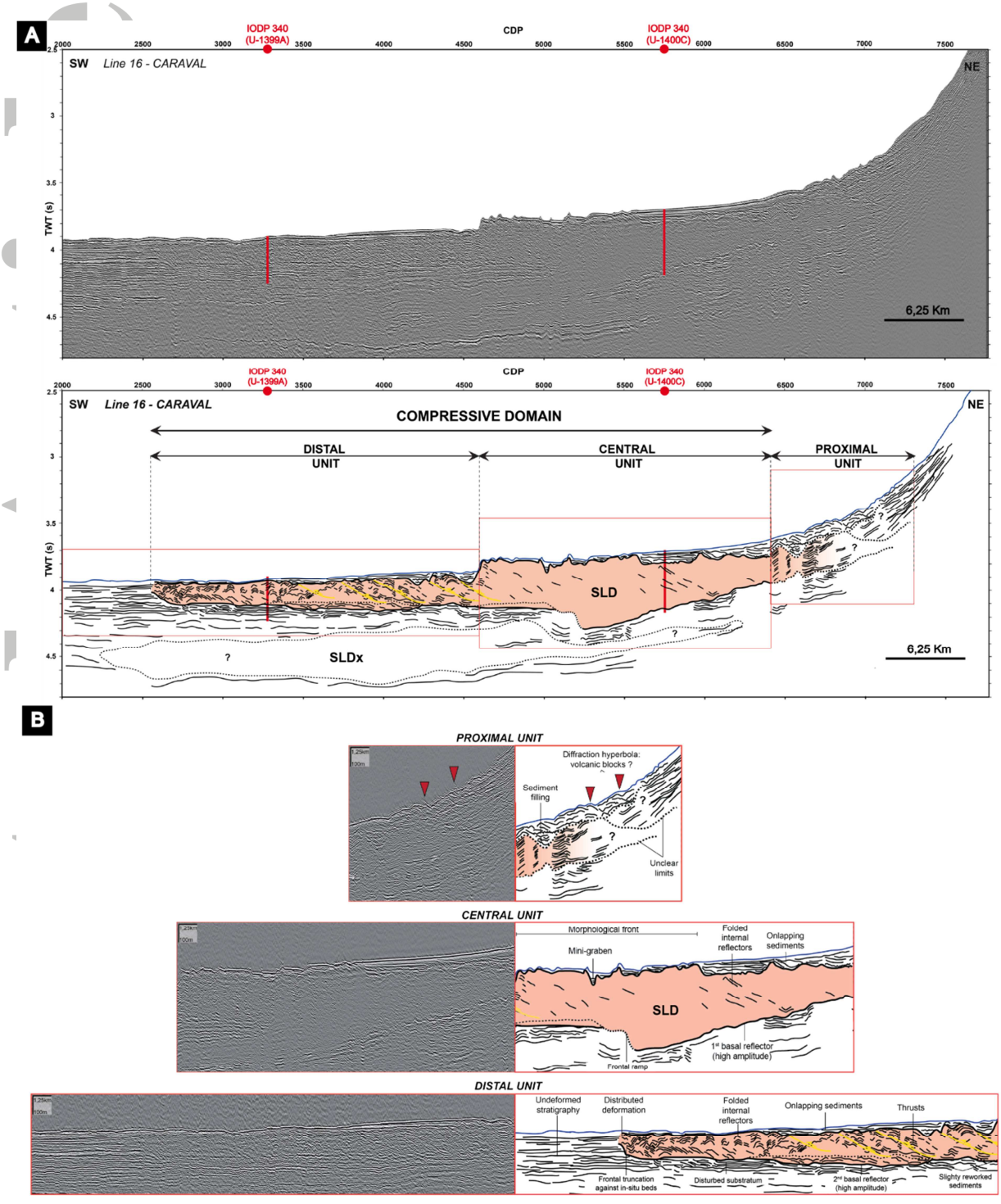

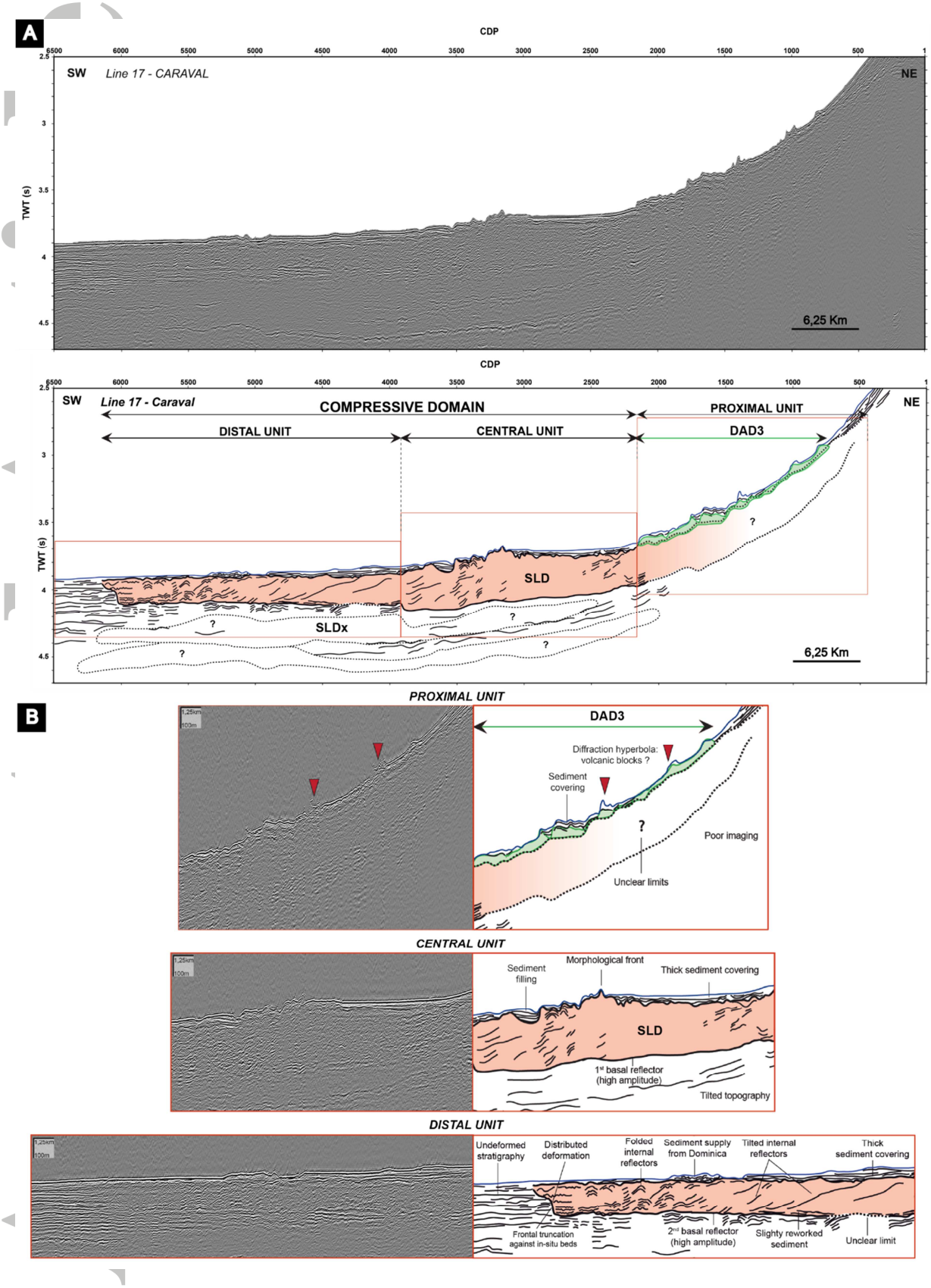

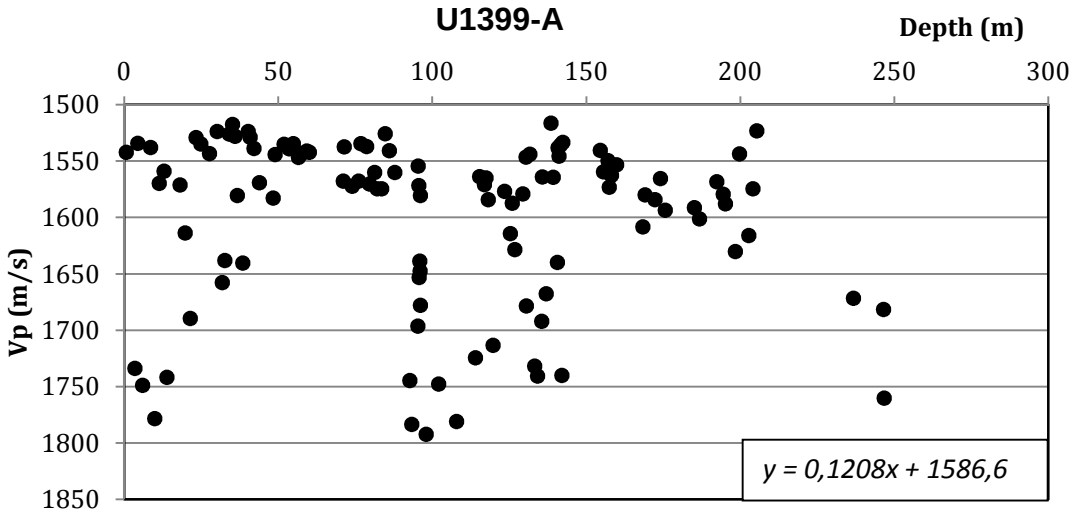

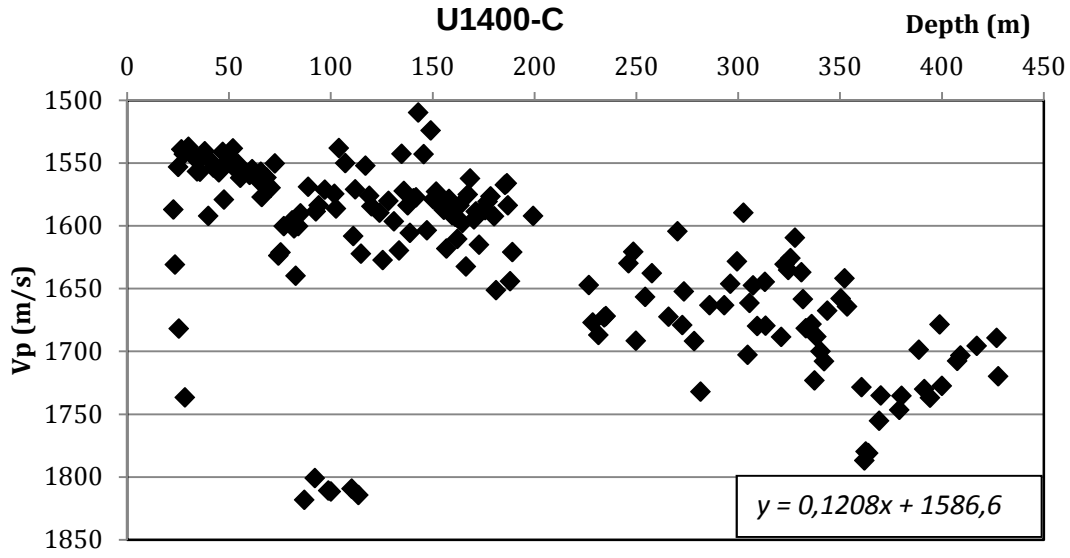

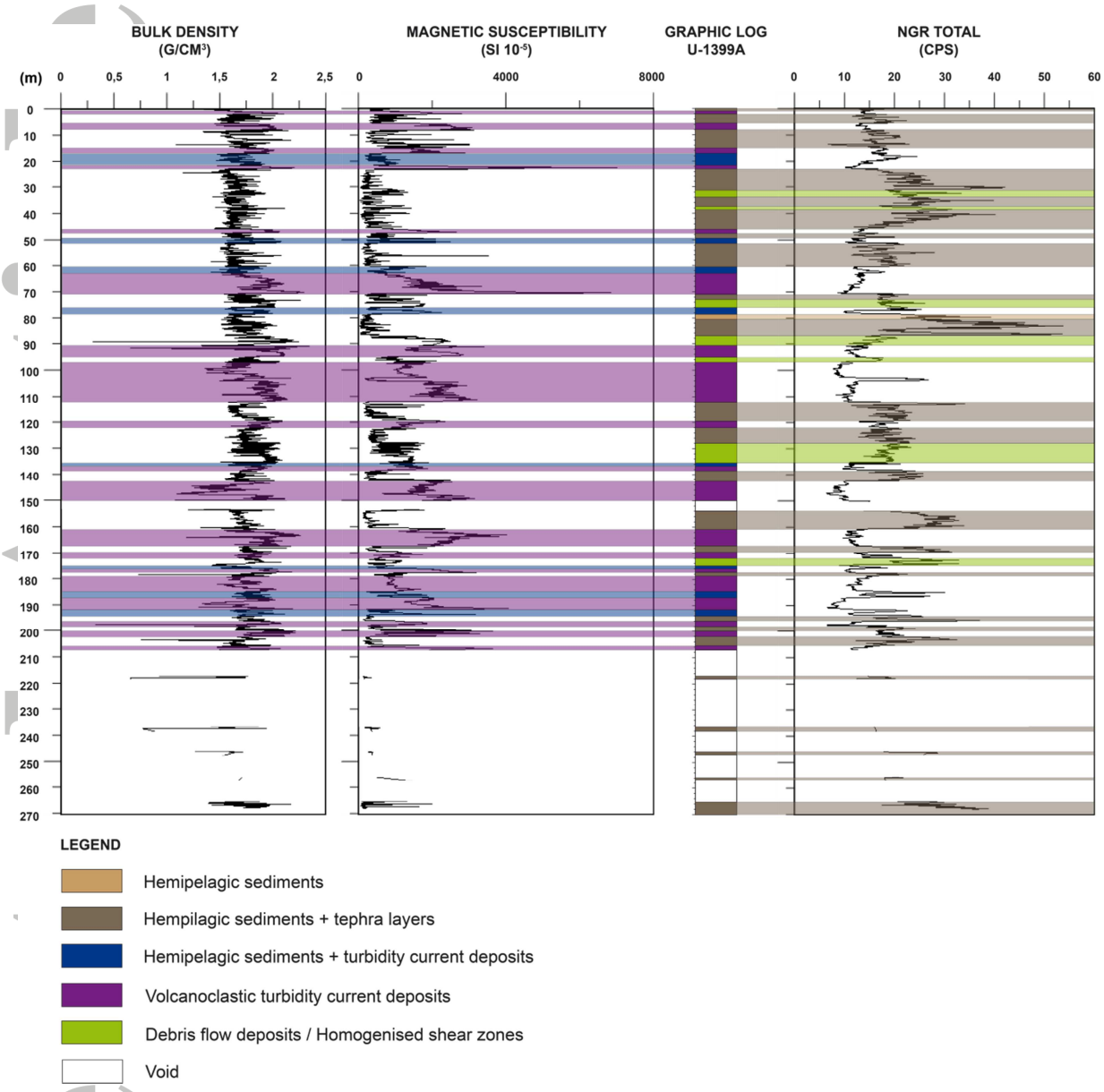

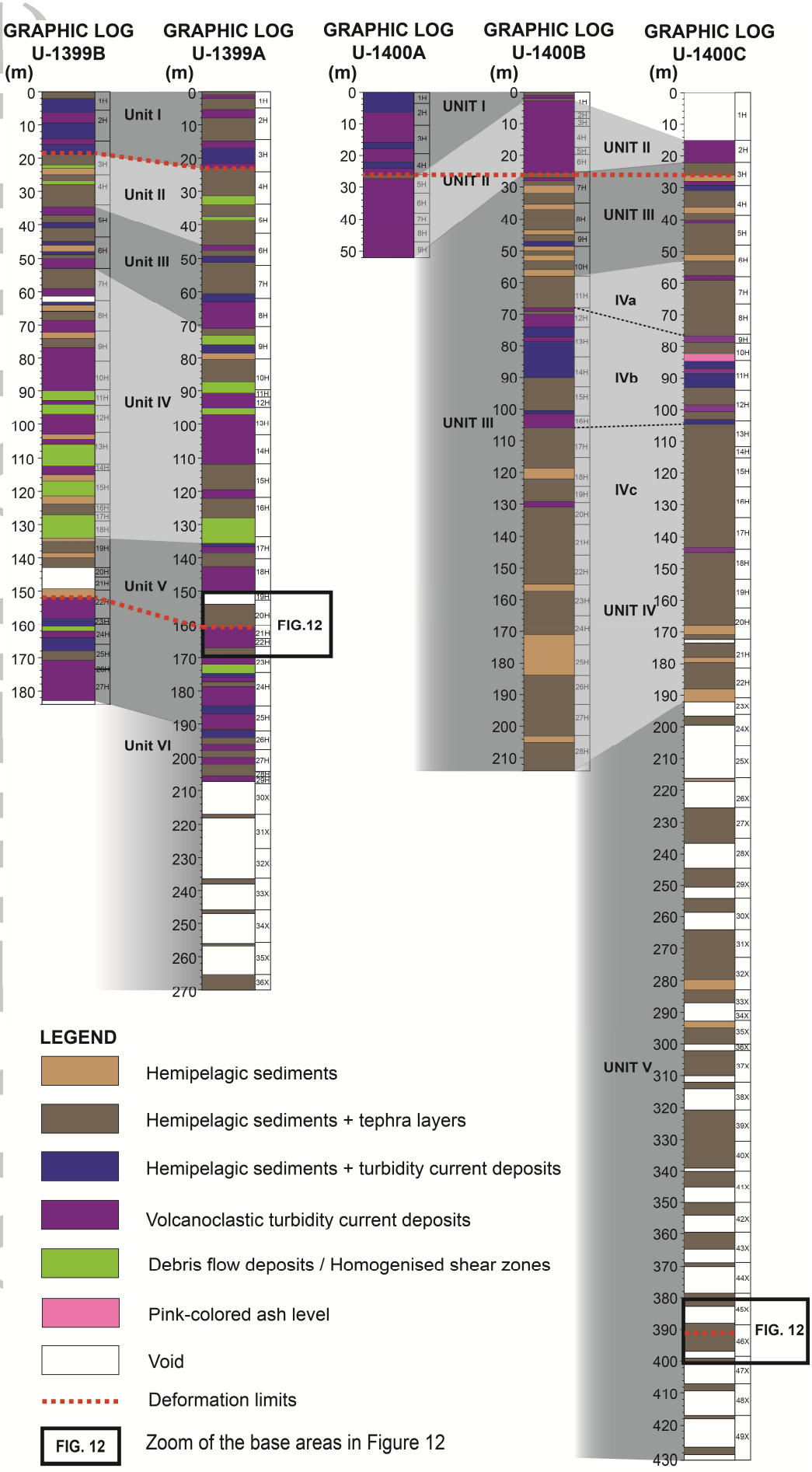

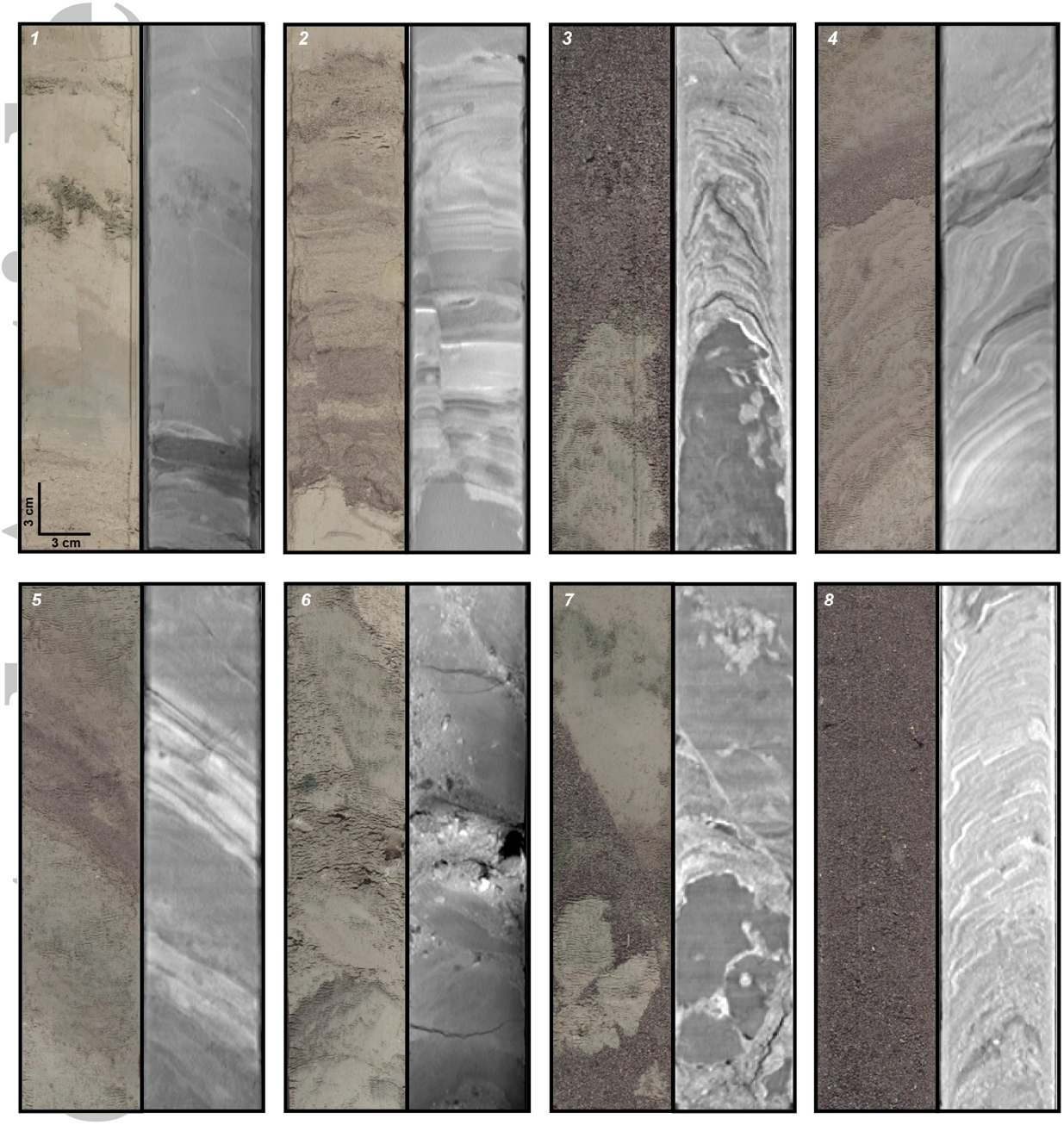

Table 2. Quantification of deformations within cores U1399-A and U1400-C. Parts of undisturbed strata are also noticed, and the turbitic deposits and void as well.

	U1399-A	U1400-C
Highly inclined and/or contorted bedding	15%	16%
Weakly inclined and/or contorted bedding	13%	12%
Alternation of highly/weakly inclined and contorted bedding in multi-directions	0%	19%
Undisturbed strata	20%	20%
Turbiditic deposits	31%	4%
Void	21%	29%